A Novel Objective Function DYNO for Automatic Multi-variable Calibration of 3D Lake Models

Wei Xia[1,2,3], Taimoor Akhtar[4], Christine A. Shoemaker[1,2,3]

[1]Department of Civil and Environmental Engineering, National University of Singapore, 117576, Singapore
[2]Department of Industrial Systems Engineering and Management, National University of Singapore, 117576, Singapore
[3]Energy and Environmental Sustainability for Megacities (E2S2) Phase II, Campus for Research Excellence and Technological Enterprise (CREATE), 138602, Singapore
[4]RWDI Consulting Engineers and Scientists, N1G 4P6, ON, Canada

Correspondence to: Wei Xia (xiawei@u.nus.edu)

Abstract. This study introduced a novel Dynamically Normalized Objective Function (DYNO) for multi-variable (i.e., temperature and velocity) model calibration problems. DYNO combines the error metrics of multiple variables into a single objective function by dynamically normalizing each variable's error terms using information available during the search. DYNO is proposed to dynamically adjust the weight of the error of each variable hence balancing the calibration to each variable during optimization search. The DYNO is applied to calibrate a tropical hydrodynamic model where temperature and velocity observation data are used for model calibration simultaneously. We also investigated the efficiency of DYNO by comparing the calibration result obtained with DYNO to the result obtained through calibrating to only temperature and to the result obtained through calibrating to only velocity. The result indicates that DYNO can balance the calibration in terms of water temperature and velocity and that calibrating to only one variable (e.g., temperature or velocity) cannot guarantee the goodness-of-fit of another variable (e.g., velocity or temperature) in our case. Our study implies that for practical application, an accurate spatially distributed hydrodynamic quantification, including direct velocity measurements are likely to be more effective than using only temperature measurements for calibrating a 3D hydrodynamic model. Our example problems were computed with a parallel optimization method PODS but DYNO can also be easily used in serial applications.

1. Introduction

Lake hydrodynamic models simulate the hydrodynamic or thermodynamic processes in lakes and reservoirs that are important for simulating water quality in aquatic eco-systems (Chanudet et al., 2012). These simulation models (e.g., hydrodynamic modelling) play a critical role in managing water bodies, as they are built to support the simulation of the spatial and temporal distributions of specific water quality variables (e.g., nutrients, chlorophyll-a), and to study the response of a water body to different future management scenarios. The parameters of these models usually need to be calibrated to measured data to adequately represent local effects and hydrodynamic processes. Model calibration is a vital step in complex hydrodynamic modelling of lakes and other aquatic systems.

Model calibration of lake hydrodynamic models is mainly done manually (also called trial and error), where experts tune the parameters and simultaneously evaluate the goodness-of-fit between the simulation output and observations. This process is subjective, time-intensive and requires extensive expert knowledge (Afshar et

al., 2011; Xia et al., 2021; Solomatine et al., 1999; Fabio et al., 2010; Baracchini et al., 2020). The challenges associated with manual calibration have encouraged the application of auto-calibration to lake hydrodynamic models, where the calibration is set up as an inverse problem to minimize the error between the simulation and observations. Some studies (e.g., Gaudard et al. (2017), Luo et al. (2018), Ayala et al. (2020) and Wilson et al. (2020)) have applied automatic calibration to one-dimensional hydrodynamic lake models where water temperature is the variable that is simulated and calibrated. These one-dimensional models are relatively cheap to run, allowing the use of automatic calibration methods that typically require many simulation evaluations to determine suitable parameter sets (e.g., differential evolution used in Luo et al. (2018) and Monte Carlo sampling used in Ayala et al. (2020)). However, one-dimensional models are unable to simulate the horizontal spatial distribution and cannot capture the 3D processes, and thus may not be suitable for certain studies. Consequently, 2-dimensional or 3-dimensional models are preferred for studying the spatial-temporal distribution of water variables and are increasingly used to study lakes around the world (Chanudet et al., 2012; Galelli et al., 2015; Hui et al., 2018; Soulignac et al., 2017; Wahl and Peeters, 2014; Xu et al., 2017; Baracchini et al., 2020) . The calibration of 3-dimensional models, though, is considerably more challenging than calibration of one-dimensional models, since 3-dimensional models are significantly more computationally expensive and also involve more complicated physical processes (such as advection of flows).

The computationally expensive character of 3-dimensional lake models makes traditional optimization methods, such as differential evolution and Monte Carlo sampling, unsuitable for automatic calibration because these methods usually require many evaluations to get an acceptable solution. Surrogate-based optimization is highly suitable for such problems (Bartz-Beielstein and Zaefferer, 2017; Lu et al., 2018; Razavi et al., 2012) and recent studies have applied surrogate-based optimization methods to parameter estimation of hydrodynamics models. Surrogate-based optimization methods use a cheap-to-run surrogate approximation model (of the calibration objective) fitted with all known (i.e., already evaluated) values of the original expensive objective function, to guide the optimization search and reduce the number of evaluations required on the expensive simulations. For example, Xia et al. (2021) proposed a new optimization method called PODS (parallel optimization with dynamic coordinate search using surrogates) suitable for computationally expensive problems, and applied it to automatic calibration of a three-dimensional lake hydrodynamic models. More elaborate discussions on surrogate-based optimization algorithms can be found in Xia et al. (2021), Xia and Shoemaker (2021), Razavi et al. (2012), Bartz-Beielstein and Zaefferer (2017) and Haftka et al. (2016).

Computational intensity is not the only critical challenge associated with parameter estimation of 3-dimensional lake hydrodynamic models. Parameter estimation of these models is also a multi-site & multi-variable calibration problem, i.e., observation data is usually available at multiple locations and the underlying models simulate multiple variables (e.g., temperature and velocity). Moreover, simultaneous calibration of multiple variables is desired due to complex interactions between the different variables. For instance, temperature and velocity are inter-dependent variables of a lake hydrodynamic model, since water temperature affects the movement of water, and water velocity affects the distribution of water temperature. However, most prior research studies have calibrated hydrodynamic models to only temperature. This might because temperature measurements are relatively less expensive to get compared with velocity measurements and often temperature measurements are available to help predict water quality phenomenon. Wahl and Peeters (2014) use the measured water temperatures to calibrate a 3-dimensional hydrodynamic model of Lake Constance. Kaçıkoç and Beyhan (2014)

calibrate the temperature of Lake Egirdir hydrodynamic model, the flow simulation of which is used for the lake water quality modeling. Marti et al. (2011) and Xue et al. (2015) also only used temperature data for lake hydrodynamic model calibration. Moreover, these studies use manual calibration for parameter estimation. Xia et al. (2021) use automatic calibration for parameter estimation, but only use water temperature observations in the calibration process. Reproducing water level is also a parameter estimation approach that pseudo-considers flow dynamics in calibration; however, a calibrated model that correctly simulates observed water level does not necessarily reproduce the observed 3D flow field accurately (Wagner and Mueller, 2002; Parsapour-Moghaddam and Rennie, 2018). Amadori et al. (2021) investigated the use of different sources of temperature data (from in suite observations, multi-site high-resolution profiles and remote sensing data) to compensate for scarcity of velocity measurements. This is a practicable approach when there is no velocity data available and there are such different sources of temperature data available. However, when there is no high-quality remote sensing data (for example because of cloud) or a large amount of high-resolution profiles of temperature measurement it is still challenging to verify the spatial simulation of hydrodynamic quantities.

Lake hydrodynamic models predict the velocities throughout a water body. Accurate velocity simulations are thus important to understand the spatial distribution of water quality problems (e.g., algal blooms) in sizeable lakes. Hence, during calibration of these models it is useful to know whether efforts to measure velocity directly are justifiable even if temperature data is already available. We will examine the extent to which direct measurement of velocities justify the extra effort by giving more accurate results for hydrodynamics models. We will also look at the error of the spatial distribution of hydrodynamics associated with calibrating to temperature only, which is rarely studied in literature.

There are a few studies that attempt to calibrate lake hydrodynamic models to both temperature and velocity. Chanudet et al. (2012) attempt to calibrate both temperature and velocity sequentially (using manual calibration), i.e., they calibrate water temperature first and then the current velocities. Baracchini et al. (2020) performed two sequential steps in the automatic calibration of temperature and velocity, and the velocity calibration is based on the results obtained from temperature calibration. However, one problem with such two-step sequential approaches, either by manual or auto-calibration is that the calibration of the second variable might significantly alter the calibration quality of the first variable. This is especially true for multi-variable calibration problems, where the multiple variables being calibrated are sensitive to the parameters being calibrated. Other examples of such multi-variable calibration problems include watershed model calibration (Franco et al., 2020) and seawater intrusion model calibration (Coulon et al., 2021) among others. These multi-variable problems require calibration frameworks that allow simultaneous calibration of all variables rather than calibrating one and then the second.

There are prior studies that simultaneously calibrate both temperature and velocity variables of hydrodynamic models. However, these use a trial and error (manual) mechanism for calibration (Råman Vinnå et al., 2017; Soulignac et al., 2017; Jin et al., 2000; Paturi et al., 2014). Manual calibration of multiple hydrodynamic variables simultaneously, is even harder than calibration of a single variable. A key challenge for automatic calibration of multi-variable calibration problems is in defining a suitable objective function. Traditional approaches typically formulate the goodness-of-fit of multiple variables into a single objective function by adding weights between the goodness-of-fit of multiple variables and solve the problem with single objective optimization (SOO) techniques (Afshar et al., 2011; Pelletier et al., 2006). However, a drawback of this approach

118   is that the relative error magnitude of each variable of the new solutions found will probably vary during the

119   search making it difficult to determine appropriate weights since they need to be determined / defined *a prior*, i.e.,

120   before optimization.

121   Another approach for calibration of multi-variables is using multi-objective optimization (MOO)

122   techniques (Afshar et al., 2013). However, multi-objective techniques are commonly used to optimize multiple

123   sub-objectives that have a trade-off between each sub-objective (Akhtar and Shoemaker, 2016; Reed et al., 2013;

124   Alfonso et al., 2010; Giuliani et al., 2016; Herman et al., 2014). While for the multi-variable hydrodynamic

125   calibration problems, it is not apparent that there is usually a trade-off between the fit of multiple variables.

126   Moreover, MOO is considerably more computationally difficult than SOO and typically requires many more

127   objective function evaluations. Thus, MOO may not be desired for computationally expensive calibration

128   problems, especially when a significant trade-off between the objectives may not be present. Consequently, multi-

129   variable calibration utilizing efficient SOO algorithms, while balancing the calibration to each variable equally

130   during calibration, is a research area of significant value.

131   We introduce a new Dynamically Normalized Objective Function (DYNO) for automatic multi-variable

132   calibration. The error of each variable (e.g., temperature and velocity of hydrodynamic models) is dynamically

133   normalized by using the information about variable error of the evaluations found during the optimization search

134   process. In this way, the balance between calibration of each variable is dynamically adjusted. We tested the

135   efficiency of DYNO on a computationally expensive hydrodynamic lake model of a tropical reservoir, which

136   takes 5 hours to run per simulation. DYNO is coupled into a recent parallel surrogate optimization algorithms

137   PODS (Xia et al., 2021) and successfully applied for the calibration of multiple variables of the hydrodynamic

138   model. Using DYNO, we investigate the impact of using temperature and/or velocity observations on model

139   accuracy. Since velocity measurements are usually not included in standard lake monitoring systems (whereas

140   temperature measurements are included), real velocity observations are seldom available (Amadori, et al, 2021).

141   We don't have real observation for the velocity data in our case as well. Hence, we did the investigation based on

142   synthetic observations generated from a calibrated model. It is worthwhile to revisit and validate this analysis with

143   real velocity measurements if they are available in future.

2. Methodology

2.1 Multi-variable Calibration Problems Description

146   The calibration problems investigated in this study are multi-site (i.e., observations are available from multiple

147   locations), multi-variable (e.g., temperature and velocity for hydrodynamics) problems, and are defined,

148   mathematically, as follows (the variable and function definition are given in Table 1):

149     $$\min_{X \in \Theta} F(X|K) = F(\{f_k(X)|k \in K\}) \tag{1}$$

150     $$f_k(X) = f_k(\{g_j(\boldsymbol{Sim}_j^k(X), \boldsymbol{Obs}_j^k)|j = 1, \cdots, M\}) \tag{2}$$

151   Note that the notation $\{z_i\}$ in Eq. (2) is simply meant to imply the function on the left depends on the finite series

152   of quantities inside the braces $\{\bullet\}$.

153   **Table 1**. Notation and definitions of variables and functions in Eq. (1) and (2).

Variable	Description

K	The set of variables whose observation data is used in calibration. For example, $K = [Tem]$ means that water temperature observation is used for calibration, i.e., water temperature is the variable that is being calibrated; $K = [\vec{Vel}]$ means velocity observation is used for calibration; $K = [Tem, \vec{Vel}]$ means that both temperature and velocity observations are used for model calibration
k	The symbol for elements in K variable (e.g., water temperature or velocity, $k = Tem$ or $k = \vec{Vel}$). $k \in K$
X	A d dimensional parameter vector restricted to parameter space Θ, where d is the number of parameters to be optimized. $X = (x_1, x_2, \ldots, x_d)$.
Θ	The parameter space is defined by the upper and lower limits on each parameter (X^{max} and X^{min}, respectively)
M	The total number of observation locations (or sites).
j	The index for observation location. $j = 1, \ldots, M$
$Sim_{t,j}^k(X)$	The simulation output of variable k at location j at time step t given the parameter vector X
$Obs_{t,j}^k$	The observation (data) of variable k at location j at time step t.
$Sim_j^k(X)$	The simulation time series output of variable k at location j at times $t = 1, \ldots, N$ given the parameter vector X. $Sim_j^k(X) = \left(Sim_{1,j}^k(X), \ldots, Sim_{N,j}^k(X)\right)$.
Obs_j^k	The observation (data) time series of variable k at location j at times $t = 1, \ldots, N$. $Obs_j^k = (Obs_{1,j}^k, \ldots, Obs_{N,j}^k)$.
N	The total time steps of the observation data
t	The index for time steps. $t = 1, \ldots, N$
Function	**Description**
$F(X\|K)$	The calibration objective function given the observation data of variables in K for calibration. $F(X\|K)$ is a composite function of $f_k(X)$
$f_k(X)$	The error function of variable k over multiple site. $f_k(X)$ is a composite function of $g_j(Sim_j^k(X), Obs_j^k)$ for sites $j = 1, \ldots, M$
$g_j(Sim_j^k(X), Obs_j^k)$	Goodness of fit between time series simulation output $Sim_j^k(X)$ and observation Obs_j^k of variable k at location j. When $k = Tem$, Normalized Root Mean Square Error (NRMSE) is utilized for $g_j(\bullet)$. When $k = \vec{Vel}$, normalized Fourier Norms of Root Mean Square Error (FNs) is used for $g_j(\bullet)$.

154

155   The set of parameters X being calibrated in this study includes nine parameters ($d = 9$). Details of these

156   parameters are provided in Table 2 in section 2.4. The two variables are calibrated in this study are velocity and

157   temperature for which data exists for different spatial location and time points.

158   We investigate different calibration formulations, where either one or both of these variables are

159   calibrated. Consequently, $K = [Tem]$ means that water temperature observation is used for calibration, i.e., water

160   temperature is the variable that is being calibrated; $K = [\vec{Vel}]$ means velocity observation is used for calibration;

161    $K = [Tem, \vec{Vel}]$ means that both temperature and velocity observations are used for model calibration, i.e., both

162   variables are being calibrated simultaneously. The objective function in each scenario is discussed in section 2.5.

2.2 DYNO for Model Calibration with Multiple Variables

164   One major issue for model calibration with multiple variables is how to formulate the error of multiple variables

165   with a single objective function. In practice, different variables (e.g., temperature and velocity) usually have

166   different physical units and magnitudes of error. Their error functions cannot be summed up directly into a single

167   objective function if we wish to give the error of each variable an equal weight in the overall objective function.

The respective error functions have to be normalized. There are goodness-of-fit metrics that can normalize the error of different variables (for example Normalized Root Mean Square Error (NRMSE) and Kling-Gupta Efficiency (KGE, (Gupta et al., 2009))). However, it is still possible that the highest attainable value (or distribution) of NRMSE (or KGE) across the parameter space for one variable maybe be much higher than the highest attainable value (or distribution) of NRMSE (or KGE) of another variable. Hence, how to balance such differences among multiple variables is still important even when the normalized goodness-of-fit metrics are used.

We propose a new general objective function, DYNO, for the multi-variable calibration problem. Let ψ be the set of evaluations found so far by the optimization, DYNO (as shown in Eq. (3)) normalizes the error of each variable $f_k(X)$ with its upper and lower bound, f_k^{max} and f_k^{min} of all evaluations in ψ. Since true values of bounds are not known, f_k^{max} and f_k^{min} are dynamically updated during the optimization search after each iteration. The Mathematical formulation of the multi-variable calibration problem, with DYNO, is as follows:

$$min\, F\,(X|K) = \sum_{k \in K} \frac{f_k(X) - f_k^{min}(X)}{f_k^{max}(X) - f_k^{min}(X)} \tag{3}$$

$$f_k^{max}(X) = \max\{f_k(X)\ for\ all\ X \in \psi\} \tag{4}$$

$$f_k^{min}(X) = \min\{f_k(X)\ for\ all\ X \in \psi\} \tag{5}$$

where $f_k^{max}(X)$ and $f_k^{min}(X)$ are the maximum and minimum values of $f_k(X)$ for all evaluations in ψ . $f_k^{max}(X)$ and $f_k^{min}(X)$ have to be updated dynamically in each iteration during optimization. The detailed description of the implementation of Eq. (3) in the algorithm (i.e., PODS) tested in this study is given in Section 2.6 (the Algorithm Description section).

2.3 Study Site and Data

We use a 3-dimensional model of a tropical reservoir as an example to test the efficiency of DYNO for multi-variable calibration problems and to study the impact of using temperature and/or velocity data for model calibration. The horizontal boundary of the studied reservoir is given in Fig. 1 (a) and (b). The reservoir has over 250 ha of water surface with the maximum depth of about 22 meters. One online water quality profiler station (STN. A1) was installed in the middle of the reservoir. The water temperature data at the station are available at various depths. The model is built for the simulation of year 2013. One-year measured temperature data is used for model calibration in a previous study (Xia et al., 2021). We use this calibrated model to create synthetic observation data since the real velocity measurements are not available. We first assume a set of "true" model parameters X^R. The value of X^R is based on manual calibration by experts and is listed in Table 2. The spatial and temporal observation data for the hypothetical lake is synthetically generated based on the "true" model parameters X^R. The synthetic observation data for the hypothetical temperate lake is generated by running the simulation model for one year with the vector of model parameters X^R. The simulation output is then saved hourly in N time steps for multiple variables, i.e., temperature and velocity ($K = [Tem, \overrightarrow{Vel}]$) at M locations (specified in Fig. 1). In our study case, $N = 8761$ and $M = 12$ with different depths of five hypothetical sensor stations (STN. A1 and STN. B1-4 as shown in Fig. 1 (a) and (b)).

The saved hourly simulated output time series is denoted as $\Gamma = \{\boldsymbol{Sim}_j^k(X^R), k \in K = [Tem, \overrightarrow{Vel}], j = 1, \dots, M\}$, which as defined (in Table 1) contains information for each time step, $t = 1, \dots, N$. So Γ is used as

204   observation data for model calibration, i.e., $Obs^k, k \in \boldsymbol{K} = [Tem, \overrightarrow{Vel}]$ in Eq. (1). In the test of optimization for

205   calibration, the true values of the parameter vector $\boldsymbol{X}^R$ are not provided to the optimization. The optimization will,

206   instead, search for a best set of $\boldsymbol{X}$ that will minimize objective function $F(\boldsymbol{X}|\boldsymbol{K})$, where $\boldsymbol{K} =$

207     $[Tem], [\overrightarrow{Vel}], or [Tem, \overrightarrow{Vel}]$. So the goal of automatic calibration via optimization is to obtain an optimum

208   calibration $\boldsymbol{X}^*$ that results in simulation model output, $\boldsymbol{Sim}_j^k(\boldsymbol{X}), k \in \boldsymbol{K}, j = 1, ..., M,$ (see Eq. (1) and Eq. (2)) that

209   is close to the synthetic observation time series data in $\boldsymbol{\Gamma}$.

210   The temperature and velocity simulation results at year 2013 based on the "true" model parameters

211   (shown in Table 2) show temporal and spatial variation, as shown in Fig. 1 (a)-(d). Figure 1 (a) and (b) show the

212   temperature and horizontal velocity distribution at the surface layer. Figure 1 (c) and (d) show the distribution of

213   temperature and velocity magnitude at STN. A1. There is obvious temperature stratification in the vertical

214   direction (as shown in Fig. 1(c)). We have five sampling locations across the reservoir. The observations data at

215   these five locations are used to calibrate the model parameters.
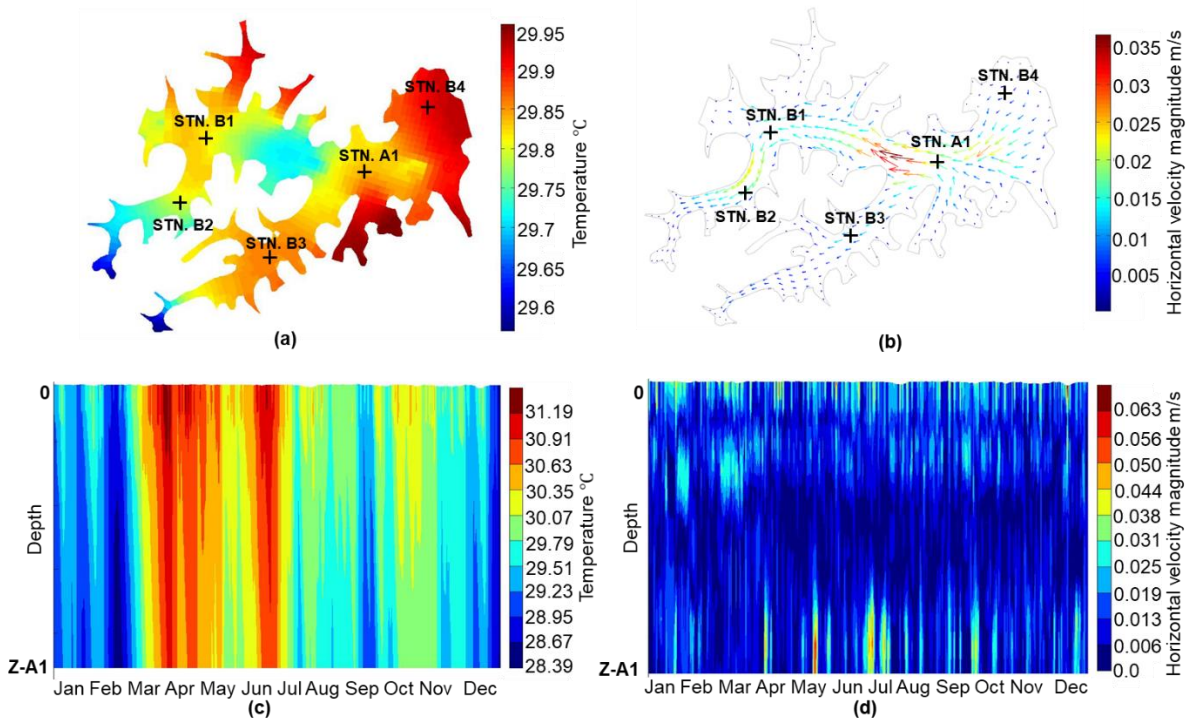
216

217   **Figure 1.** Hydrodyanmic model simulation result (with "true" model parameters) at year 2013. (a) Simulated
218   temperature spatial distribution with sampling locations. (b) Simulated velocity spatial distribution with sampling
219   locations. (c) Time-depth plot of simulated temperature at STN. A1. (d) Time-depth plot of velocity magnitude at
220   STN. A1. Z-A1 is the maximum water depth at station A1.

221   **2.4 Hydrodynamic Model and Calibration Parameters**

222   The description of the hydrodynamic model is given in (Xia et al., 2021). The hydrodynamic model is built with

223   Delft3D-FLOW (Hydraulics, 2006). The Delft3D-Flow hydrodynamic model used was set up by the water

224   utilities' employees and consultants, including the domain construction, input data preparation, and model

225   configuration. The grid coordinate system is based on Cartesian coordinates (Z-grid), which has horizontal co-

226   ordinate lines that are almost parallel with density interfaces to reduce artificial mixing of scalar properties such

227   as temperature. The number of grid points in the x-direction is 65, the number of grid points in the y-direction is

228 67, and the number of layers in vertical is 19. A single 1-year simulation takes about 5 hours to run in serial on a

229 windows desktop with CPU Intel Core i7-4790.

230 There are nine tunable model parameters (listed in Table 2) in the model. The first five parameters in

231 Table 2 are related to the turbulence calculation. The k-ε closure model (Uittenbogaard et al., 1992) was chosen

232 as the turbulence closure model to calculate the viscosity and diffusivity of the water. The calculation of the

233 viscosity and diffusivity involves five parameters: 1) background viscosity in horizontal v_H^{back} , 2) vertical v_V^{back},

234 3) the background eddy diffusivity in horizontal D_H^{back} , 4) vertical D_V^{back} and 5) the Ozmidov length L_{oz}. These

235 parameters affect both the velocity and the temperature. The vertical exchange of horizontal momentum and mass

236 is affected by vertical eddy viscosity and eddy diffusivity coefficients (Elhakeem et al., 2015). The horizontal

237 velocities are affected by the horizontal eddy viscosity and diffusivity coefficients (Chanudet et al., 2012).

238 Chanudet et al. (2012) highlighted that the most impactful parameter for temperature is the background vertical

239 eddy viscosity and the Ozmidov length L_{oz} also has a significant effect on the thermal stratification by affecting

240 the vertical temperature mixing.

241 The next three parameters in Table 2 are related to the simulation of surface heat flux. In the heat flux

242 model, the evaporative heat flux and heat convection by forced convection are parameterized by the Dalton

243 number c_e and Stanton number c_H , respectively, which are also in the list of calibration parameters. The Secchi

244 depth H_{Secchi} (also included in Table 2) is another parameter required by the Ocean heat flux model. Secchi depth

245 is related to the transmission of radiation in deeper water and thus affects the vertical distribution of heat in the

246 water column (Chanudet et al., 2012). Heat fluxes through the reservoir bottom were not simulated in the current

247 model. The last parameter is the Manning coefficient, which affects the roughness of the bottom of the lake and

248 has a direct impact on velocity.

249 All these nine parameters affect (either directly or indirectly) the thermal and current activity in the water

250 body. These are also the parameters included in the routine model calibration by local experts and thus, are

251 included in the calibration process in our study. The calibration range for these parameters (given in Table 2) is

252 suggested by Singapore water utilities employees and consultants. Some of these parameters might be

253 spatiotemporally variant (such as Secchi depth, Ozmidov length scale, Dalton number, and Stanton number).

254 Considering these parameters as time or space-varying parameters will substantially increase the number of

255 decision variables in optimization. Considering that the reservoir in our study is relatively small and it is located

256 in a tropical region where there is no significant seasonal variation, we consider assume these parameters to be

257 constant across space and time.

258 **Table 2.** Model parameters used in calibration. X^R denotes the true solution used to generate synthetical
259 temperature and velocity observations at multi-sites.

Parameter vector X	Parameter	Description (unit)	Physical process	Range	X^R
x_1	v_H^{back}	Background viscosity in horizontal (m²/s)		0.1-1.0[a,b,d,e]	0.5
x_2	D_H^{back}	Background eddy diffusivity in horizontal (m²/s)	3D turbulence	0.1-1.0[a,b,d,e]	0.5
x_3	v_V^{back}	Background viscosity in vertical (m²/s)		0-0.005[a,b,c,e]	5.00E-05

x_4	D_V^{back}	Background eddy diffusivity in vertical (m²/s)		0-0.005 [a,b,c,e]	5.00E-05
x_5	L_{oz}	Ozmidov length scale (m)		0-0.05 [a,b, e]	0.015
x_6	H_{Secchi}	Secchi depth (m)		0.1-2.0 [a,e,f]	1
x_7	c_e	Dalton number (-)	Heat flux	0.001-0.002 [a,b,c,e]	0.0013
x_8	c_H	Stanton number (-)		0.001-0.002 [a,b,c,e]	0.0013
x_9	n	Manning coefficient (m⁻¹ᐟ³s)	Roughness	0.02-0.03 [a,b,e]	0.022

[a]Deltares (2014); [b]Chanudet et al. (2012); [c]Wahl and Peeters (2014); [d]Råman Vinnå et al. (2017); [e]Soulignac et al. (2017); [d]Pijcke (2014)

2.5 Calibration Problem Formulation

Three scenarios are considered to investigate the impact of model calibration against temperature and/or velocity observations (as discussed in section 2.1). The first two scenarios calibrate to only one variable, and the last scenario calibrates both variables simultaneously. This section give the detailed calibration formulations of these three scenarios.

2.5.1 Model Calibration with One Variable

The objective functions for Cali-Tem and Cali-Vel scenarios are summarized in Eq. (6)-(8) and Eq. (9)-(11), respectively, where only observations of one variable are included in the calibration.

$$F(\mathbf{X}|\mathbf{K} = [Tem]) = f_{Tem}(\mathbf{X}) \tag{6}$$

$$f_{Tem}(\mathbf{X}) = \sum_{j=1}^{M} NRMSE_j^{Tem}(\mathbf{X}) \tag{7}$$

$$NRMSE_j^{Tem}(\mathbf{X}) = \frac{\sqrt{\frac{1}{N}\sum_{t=1}^{N}\left[Sim_{t,j}^{Tem}(\mathbf{X}) - Obs_{t,j}^{Tem}\right]^2}}{\frac{1}{N}\sum_{t=1}^{N} Obs_{t,j}^{Tem}} \tag{8}$$

$$F(\mathbf{X}|\mathbf{K} = [\overrightarrow{Vel}]) = f_{\overrightarrow{Vel}}(\mathbf{X}) \tag{9}$$

$$f_{\overrightarrow{Vel}}(\mathbf{X}) = \sum_{j=1}^{M} FNs_j^{\overrightarrow{Vel}}(\mathbf{X}) \tag{10}$$

$$FNs_j^{\overrightarrow{Vel}}(\mathbf{X}) = \frac{\sqrt{\frac{1}{N}\sum_{t=1}^{N}\left\|Sim_{t,j}^{\overrightarrow{Vel}}(\mathbf{X}) - Obs_{t,j}^{\overrightarrow{Vel}}\right\|_2^2}}{\sqrt{\frac{1}{N}\sum_{t=1}^{N}\left\|Obs_{t,j}^{\overrightarrow{Vel}}\right\|_2^2}} \tag{11}$$

where, $NRMSE_j^{Tem}(\mathbf{X})$ and $FNs_j^{\overrightarrow{Vel}}(\mathbf{X})$ denote the Normalized Root Mean Square Error (NRMSE) of temperature (described in Eq. (8)), and normalized Fourier Norms (FNs) of velocity vectors (described in Eq. (11)) at locations j. $Sim_{t,j}^{\overrightarrow{Vel}}(\mathbf{X})$ and $Obs_{t,j}^{\overrightarrow{Vel}}$ denote the simulated velocity given a parameter vector $\mathbf{X}$ and observed velocity, respectively, at time step t and location j. $Sim_{t,j}^{\overrightarrow{Vel}}(\mathbf{X})$ and $Obs_{t,j}^{\overrightarrow{Vel}}$ are 3-dimensional vector. $\|-\|_2$ in Eq. (11) is the Euclidean norm used to quantify the size of a vector.

The temperature and velocity data are taken at different depths of multiple stations, and their magnitude at different locations might be different due to spatial variation. Hence, the fitness at each location should be normalized before being summed into the objective function. For water temperature, Normalized Root Mean Square Error (NRMSE, as described in Eq. (8)) is used to quantify and normalize the error between the simulated and observed data. For velocity, normalized Fourier Norms of RMSE (FNs, as described in Eq. (11)) are used to

287 measure the error between the model-simulated and observed data (corresponding simulated and observed
288 velocity data points are three-dimensional vectors). The calculation of the Fourier Norm follows the description
289 in Beletsky et al. (2006), Huang et al. (2010), Paturi et al. (2014) and Råman Vinnå et al. (2017).

2.5.2 DYNO for Model Calibration with Multiple Variables

291 In the Cali-Both scenario, both temperature and velocity are calibrated simultaneously, which can be treated as a
292 bi-objective function problem. The objective function in the Cali-Both scenario (as shown in Eq. (12)) applies the
293 DYNO proposed in Eq. (3). The error functions for water temperature, i.e., $f_{Tem}(\boldsymbol{X})$, and velocity, i.e., $f_{\overrightarrow{Vel}}(\boldsymbol{X})$,
294 are the objective functions of the Cali-Tem scenario (Eq. (7)) and the Cali-Vel scenario (Eq. (10)), respectively.
295 The temperature and velocity errors are dynamically normalized with their upper and lower bounds during the
296 search of the optimization algorithm before being summed into a single objective function. The mathematical
297 formulation of the objective function in the Cali-Both Scenario (based on Eq. (3)) is as follows:

$$298 \quad F(\boldsymbol{X}|\boldsymbol{K} = [Tem, \overrightarrow{Vel}]) = \frac{f_{Tem}(\boldsymbol{X}) - f_{Tem}^{min}(\boldsymbol{X})}{f_{Tem}^{max}(\boldsymbol{X}) - f_{Tem}^{min}(\boldsymbol{X})} + \frac{f_{\overrightarrow{Vel}}(\boldsymbol{X}) - f_{\overrightarrow{Vel}}^{min}(\boldsymbol{X})}{f_{\overrightarrow{Vel}}^{max}(\boldsymbol{X}) - f_{\overrightarrow{Vel}}^{min}(\boldsymbol{X})} \qquad (12)$$

299 where the maximum and minimum of $f_{Tem}(\boldsymbol{X})$ and $f_{\overrightarrow{Vel}}(\boldsymbol{X})$ are updated after each optimization iteration (since
300 new parameter sets are sampled in each optimization iteration). As the number of iterations increases, the
301 denominators in Eq. (12) also increase since the optimization method finds better minimum objective function
302 values. Hence the individual objective function components (for each variable) scale dynamically to maintain an
303 approximately equal weight of the terms related to temperature and velocity.

304 As defined in Eq. (6) to Eq. (12), three calibration formulations are investigated in this study. Table 3
305 gives a summary of these calibration formulations.

306 **Table 3**. Summary of Objective function formulations for different calibration scenarios.

Scenario Name	Variables used for calibration	Objective Function	Objective Function Formula
Cali-Tem	Temperature	$F(\boldsymbol{X}|\boldsymbol{K} = [Tem])$	Eq. (6)~(8)
Cali-Vel	Velocity	$F(\boldsymbol{X}|\boldsymbol{K} = [\overrightarrow{Vel}])$	Eq. (9)~(11)
Cali-Both	Temperature and Velocity	$F(\boldsymbol{X}|\boldsymbol{K} = [Tem, \overrightarrow{Vel}])$	Eq. (12)

2.6 Implementation of DYNO with PODS

308 In this section we describe the implementation details for incorporating DYNO into a new efficient parallel
309 surrogate optimization algorithm, PODS (described in Fig. 2). PODS (Xia et al., 2021) is a parallel version of the
310 serial DYCORS (DYnamic COordinate search using Response Surface models) algorithm introduced by (Regis
311 and Shoemaker, 2013). DYCORS is an iterative surrogate method (such methods are sometimes also called
312 Response Surface Optimization methods, where cheap surrogates of expensive objective are built to improve
313 optimization efficiency), designed for optimization of computationally expensive black-box functions within a
314 limited number of evaluations. DYCORS uses RBF (Radial Basis Function) as surrogates to efficiently explore
315 the parameter space and propose promising new solutions for expensive evaluation in each algorithm iteration.
316 The RBF-guided search methodology of DYCORS is designed for high-dimensional black-box optimization

within a limited number of evaluations of computationally expensive real objective functions. PODS, like DYCORS, is designed for black-box optimizations problems that are high-dimensional and computationally expensive and have multiple local minima. Xia et al. (2021) show that PODS is considerably more efficient than other parallel global optimization methods in obtaining good solutions with fewer objective function evaluations, which is very important for expensive objective functions like hydrodynamics models. PODS parallelized the serial DYCORS algorithm by following the Mater-worker framework (as shown in Fig. 2). This parallelization strategy of the algorithm allows simultaneous function evaluations on multiple processors (cores) in batch mode, which reduced the wall-clock time of the optimization process. This can greatly speedup the calibration of computationally expensive models and make the calibration of some extremely expensive models computationally tractable.

The PODS algorithm begins the optimization from an initial experiment design where a random initial set of evaluations points are generated with the Latin Hypercube Design (LHD). These evaluation points are distributed randomly to P workers for simulation evaluations. Each worker will calculate the error/ objective function of each variables $\{f_k(X_i)|k \in K\}$ based on Eq. (2) and return them back to the master. This step (W3 in Fig. 2) for DYNO-based PODS is different from the original PODS. In the original PODS, only the final objective function value (instead of error of each variables) is returned to master.

After the master collects the result of all the P evaluations, it will add these new results into the history list ψ that saves all evaluation results found in previous iterations. The history list of ψ is not in the original PODS and it is necessary for the calculation of the DYNO objective function ($F(X|K)$, X) (as shown in Eq. (3)). For instance, the maximum and minimum value of the error of each variable $f_k^{max}(X)$ and $f_k^{min}(X)$ are dynamically changing with the increase of the history list ψ. The objective function value $F(X|K)$ for all evaluations found in current and previous iterations need to be recalculated because of the update of $f_k^{max}(X)$ and $f_k^{min}(X)$. And the best solution found so far is identified based on newly calculated $F(X|K)$. When only one variable (e.g., temperature or velocity) is considered in the objective function, the best solution is the evaluation with the lowest error between the simulation output and observations of the variable considered. In cases where multiple variables are considered in calibration, the best solution should be the evaluation with smallest value of $F(X|K)$ after considering the error of multiple variables (as shown in Eq. (3)). Because the change of objective function value for all evaluations in ψ, the RBF is also rebuilt with these new objective function values of all evaluated solutions ($F(X|K)$, X). The rebuilt RBF surrogate is used for the generation of the evaluation points for the next iteration.

PODS with DYNO implementation uses the RBF surrogate in the same way as the original PODS does. PODS first generates a large number of candidate points around the best solution found so far (refer to Section 2.2 in Xia et al (2021)). The algorithm then selects P evaluation points from these candidate points based on their estimated objective function $\hat{F}(X|K)$ based on RBF surrogate and the minimum distance from all previous evaluation solutions in ψ. A lower estimated objective function $\hat{F}(X|K)$ is better since it more likely to lead to solutions with lower objective function value. Meanwhile, candidate points that are far from previous solutions are also preferred since they help the algorithm to explore regions of the solution domain that not explored in previous iterations. These unexplored regions could possibly be regions where better solutions are located. The consideration of estimated objective function $\hat{F}(X|K)$ and distance information are both considered when

356 selecting the candidate points through a weighted score based on these two aspects. For detailed information on
357 implementation of evaluation point selection criteria, one can refer to Section 2.3 in Xia et al (2021). The selected
358 *P* evaluation points are then distributed to *P* workers for evaluations and the iteration loop continues until the
359 stopping criteria is met (e.g., the computing budget finished.)

360 In summary, the implementation of DYNO affects the selection of the best solution found so far and also
361 the surrogate model (These steps are W3 and M1-5, as highlighted in green color in Fig. 2).We should highlight
362 that thefitting of the surrogate model is computationally inexpensive compared with the runtime of the expensive
363 objective function. Hence it does not affect overall algorithm runtime.

364
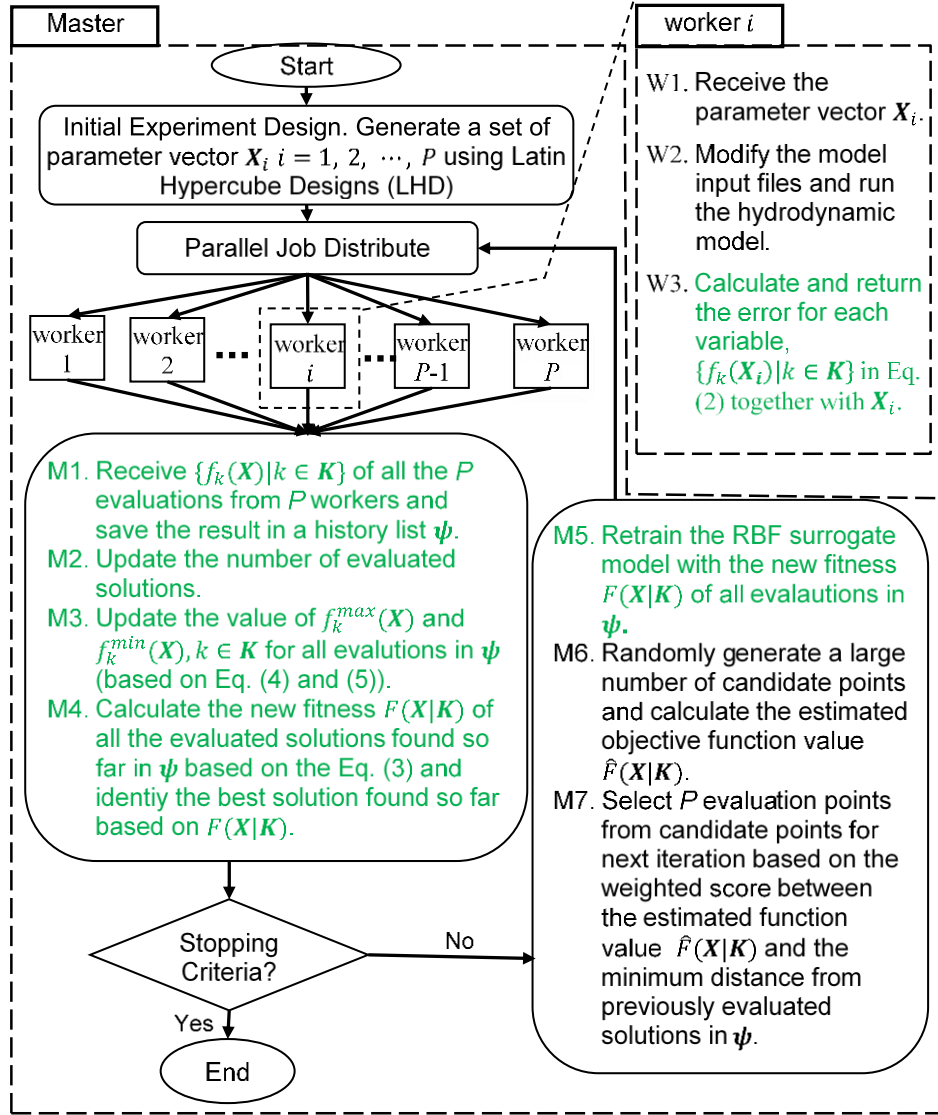
365
366 **Figure 2.** Diagram of the implementation of DYNO with the parallel algorithm PODS. *P* is the number of
367 processors available. The green texts (i.e., steps W3, M1-5) are changes made on PODS to incorporate DYNO.
368 The rest part follows the original PODS method.

369 **2.7 Experiments Setup**

370 All computational experiments in this study are implemented on a single node on the National Supercomputer
371 Center (NSCC) of Singapore, which is a Linux-based platform with dual Intel Xeon E5-2690 v3 Processors, with
372 each node having 24 cores. Hence, we set the number of processors *P* to be 24. Due to the stochastic nature of the

373 optimization algorithm (i.e., PODS) used in this study, multiple optimization runs are executed for each calibration
374 experiment in Table 3. Considering that the calibrated hydrodynamic model in this study is extremely expensive,
375 we perform three optimization trials for each calibration experiment (see Table 3 for a list of experiments).
376 Furthermore, to remove any initial sampling bias, each concurrent optimization trial for the three calibration
377 experiments is initialized with the same Latin Hypercube experimental design (so the calibration in each scenario
378 is starting from the same initial solutions). We also investigated the performance of different forms of DYNO on
379 the Cali-Both scenario.

380 We set the same evaluation budget (i.e., the maximum number of hydrodynamic model runs) for each
381 trial and calibration scenario (i.e., Cali-Tem, Cali-Vel, and Cali-Both). The maximum number of hydrodynamic
382 model runs in each trial is 192, which is about 8 iterations with 24 evaluations in each iteration. Our result indicates
383 that 8 iterations are a sufficient calibration budget, as the calibration progress plot in Figure S1 shows that the
384 optimization experiments almost converged in the last few iterations.

385 The computational time of one simulation is approximately 5 hours on a windows desktop with a CPU
386 Intel Core i7-4790 processing unit. However, when running 24 simulations simultaneously on the multi-core
387 platform, the computational time gets longer because of the limited cache memory resources (as discussed in Xia
388 and Shoemaker (2022)). Cache memory is a small amount of much faster memory than main memory. The wall-
389 clock time for one iteration with 24 cores simultaneously running is about 12 hours if using the default process
390 scheduling of the nonuniform memory access (NUMA) multi-core system. We used the mixed affinity scheduling
391 proposed by Xia and Shoemaker (2022), and the wall-clock time is reduced to about 8 hours per iteration. The
392 mixed affinity scheduling changed the default affinity setting by setting a hard affinity on the simulation of each
393 PDE model (i.e., fixing the process of each PDE simulation to one core). This approach proved to be efficient for
394 memory usage and reduced the simulation time. More details about the mixed affinity scheduling and the NUMA
395 system can be found in the study of Xia and Shoemaker (2022). Hence, the wall-clock time of each trial takes
396 about 64 hours (8 iteration×8 hours/iteration).

3. Numerical Results and Discussion

3.1 Comparison of Calibrating to Temperature and/or Velocity

3.1.1 Final Solutions in Goodness-of-fit Metrics

400 We first compare the three calibration formulations in terms of goodness-of-fit metrics for both temperature and
401 velocity. Table 4 summarizes this comparison for the three formulations, i.e., i) Cali-Tem, ii) Cali-Vel and iii)
402 Cali-Both (see definition in Table 3), with PODS used as the optimization algorithm and with a budget of 192
403 simulations.

404 The mean as well as the standard deviation of both temperature error $f_{Tem}(X^*|K)$ (calculated as Eq. (7))
405 and velocity error $f_{\overline{Vel}}(X^*|K)$ (Calculated as in Eq. (10)) over three trials are reported in Table 4, for all three
406 calibration scenarios. X^* in Table 4 denotes the optimal calibration solution obtained by PODS in each trial for a
407 given scenario (defined by the set of variables K). The solution with the lowest variable error ($f_{Tem}(X^*)$
408 or $f_{\overline{Vel}}(X^*)$) is highlighted in bold in Table 4. Table 4 reports the variable errors of both temperature and velocity
409 for all formulations to understand the impact of ignoring or including a variable in the calibration formulation.

410   Please note that the temperature error, $f_{Tem}(X|K = [Tem])$, reported in Table 4, is exactly the calibration

411   objective function in the Cali-Tem scenario ($F(X|K = [Tem])$ as shown in Eq. (7)). Similarly, the velocity error

412     $f_{\overrightarrow{Vel}}(X|K = [Tem])$ is exactly the calibration objective function in the Cali-Vel scenario (i.e., $F(X|K = [\overrightarrow{Vel}])$

413   as shown in Eq. (10)). We use the word variable error instead of objective function value when referring to the

414   values in Table 4 in subsequent discussions since we are in part looking at the impact of using data from one

415   variable to predict another variable for which we don't have data. It also worth mentioning that the value in Table

416   4 is a sum of temperature or velocity error at multiple (in total 12) locations. Hence the error at each location is

417   smaller than the value in the table.

418   Table 4 shows that the solution obtained when calibrating to temperature observation only (Cali-Tem)

419   has smaller temperature errors but larger velocity errors than that if calibrating to velocity observation data only

420   (Cali-Vel). However, it is surprising that when calibrating to both temperature and velocity (Cali-Both), the

421   solution obtained by PODS has the lowest temperature and lowest velocity error compared with calibrating to

422   either temperature observation or velocity observation only. This might be because calibrating to temperature will

423   help to improve the fit of velocity and vice versa. This makes sense because water temperature and velocity are

424   two related variables in hydrodynamic modeling, and they are affecting each other. Velocity is the fundamental

425   variable of hydrodynamics with directional information not provided by temperature; temperature (via the heat

426   flux model) may also affect the velocity field since it affects water density. This might explain calibrating both

427   temperature and velocity simultaneously gives the best results. Our analyses here are based on physical models,

428   which are built based on physics laws and knowledge human have learned over hundreds of years. Our findings

429   here are in line with the study of Baracchini et al (2020), where they also suggested have both temperature and

430   velocity for a complete system calibration.

431 **Table 4.** Summary table of the solution obtained by PODS for each scenario (Cali-Both, Cali-Vel, and Cali-Tem).
432 $f_{Tem}(X^*|K)$ and $f_{\overrightarrow{Vel}}(X^*|K)$ are the temperature error $f_{Tem}(X^*)$ and velocity error $f_{\overrightarrow{Vel}}(X^*)$ (calculated in Eq. (7)
433 and Eq. (10), respectively, with the optimal solution X^* obtained in each trial). The mean and standard deviation
434 of $f_{Tem}(X^*|K)$ and $f_{\overrightarrow{Vel}}(X^*|K)$ among three trials are reported. The variable error is bolded in each scenario when
435 the observation of the variable is included in the calibration in each scenario. (Some terms defined in Table 1)

Scenarios	The composite error of each variable (Temperature or Velocity)	
	$f_{Tem}(X^*|K)$ Mean (Std.)	$f_{\overrightarrow{Vel}}(X^*|K)$ Mean (Std.)
Cali-Both $K = [Tem, \overrightarrow{Vel}]$	**0.014 (0.003)**	**1.939 (0.165)**
Cali-Vel $K = [\overrightarrow{Vel}]$	0.087 (0.023)	2.809 (0.319)
Cali-Tem $K = [Tem]$	0.024 (0.005)	5.888 (1.435)

436 **3.1.2 Visual Comparison of Calibration Errors**

437   The above analysis is based on the average variable error statistics only (i.e., $f_{Tem}(X^*|K)$ and $f_{\overrightarrow{Vel}}(X^*|K)$), of the

438   best results obtained from PODS (over multiple trials) for all calibration scenarios. In order to further analyze the

439   difference between calibration formulations (in terms of their effectiveness in calibrating both temperature and

440   velocity), we visually compare the best calibration solutions (X^*) obtained by PODS for each scenario, i.e., Cali-

441   Tem, Cali-Vel and Cali-Both. We select one representative optimal solution (X^*) from 3 trials in each scenario

442   for this comparison. An initial uncalibrated solution is included in the comparison. The parameter value of the

443   uncalibrated solution (in Table S1) is set be the middle of the calibration range in Table 2.

444   The objective function value in terms of temperature and velocity composite error (over multiple

445 locations) ($f_{Tem}(\boldsymbol{X})$ and $f_{\overrightarrow{Vel}}(\boldsymbol{X})$, as formulated in Eq. (7) and (10), respectively) and the corresponding parameter

446 configuration ($\boldsymbol{X}^*$) of the selected solution (among three trials) are plotted in Fig. 5 and reported in Table S1. In

447 general, the solution in the Cali-Both scenario is closer to the True solution than solutions in other two scenarios.

448 The solution in the Cali-Both scenario is closest to the True solution at four parameters (i.e., $\boldsymbol{D_H^{back}}$, $\boldsymbol{D_V^{back}}$, $\boldsymbol{H_{Secchi}}$,

449 $\boldsymbol{c_H}$). In addition, besides the Manning coefficients, the solution in the Cali-Both scenario is not the worst at any

450 parameter. In contrast, solution in the Cali-Tem in worst at five parameters (i.e., $\boldsymbol{v_H^{back}}$, $\boldsymbol{D_H^{back}}$ $\boldsymbol{v_V^{back}}$, $\boldsymbol{D_V^{back}}$, $\boldsymbol{c_e}$)

451 and solution in the Cali-Vel is worst at $\boldsymbol{L_{oz}}$, $\boldsymbol{H_{Secchi}}$, $\boldsymbol{c_H}$. This indicates that calibrating to both temperature and

452 velocity can help to prevent very bad value of the 9 calibration parameters.

453   The horizontal velocity error $\Delta\overrightarrow{Vel}$ (2-dimensional) between simulated velocity $Sim_{t,j}^{\overrightarrow{Vel}}(\boldsymbol{X}^*)$ and

454 observed velocity $Obs_{t,j}^{\overrightarrow{Vel}}$ (in the horizontal plane) is plotted as scatter plots of time-series in Fig. 3 (for all

455 calibration scenarios). The temperature error ΔTem between simulation temperature $Sim_{t,j}^{Tem}(\boldsymbol{X}^*)$ and observed

456 temperature $Obs_{t,j}^{Tem}$ is plotted as a time series (for each calibration scenario) in Fig. 4.

457   The error plots for the two sampling locations at multiple depths (i.e., surface layers of station STN. A1

458 and STN. B1 as shown in Fig. 1 (a)) are visualized in Fig. 3 and 4 (for one year). Since the velocity error $\Delta\overrightarrow{Vel}$ at

459 a particular time and location is a vector (and not a scalar like temperature) and velocity error in 3 dimensions (for

460 a time-series) is hard to represent visually, Fig. 3 only plots the velocity error (for one year) $\Delta\overrightarrow{Vel}$ in the horizontal

461 plane (i.e., X and Y directions only). Moreover, each dot represents the error at one point in time within the study

462 period.

463   Figure 3 plots the difference between the simulated velocity (for the optimized parameter values obtained

464 from Cali-Tem (red scatter points), Cali-Vel (black scatter points), and Cali-Both (blue scatter points) scenarios)

465 and observed velocity. Ideally, the error for each scatter point should be zero, i.e., at the intersection of the two

466 lines. Figure 3 illustrates that calibrating to temperature data only (red scatter plot) results in larger velocity error

467 $\Delta\overrightarrow{Vel}$, relative to velocity error when calibrating to velocity data only (Cali-Vel scenario, i.e., black scatter plot)

468 or to both velocity and temperature data (Cali-Both scenario, i.e., blue scatter plot). Figure 3 also shows that

469 solutions of all the three scenarios improved the temperature fit compared with the initial solution, which

470 demonstrate the effectiveness of the optimization calibration.

471
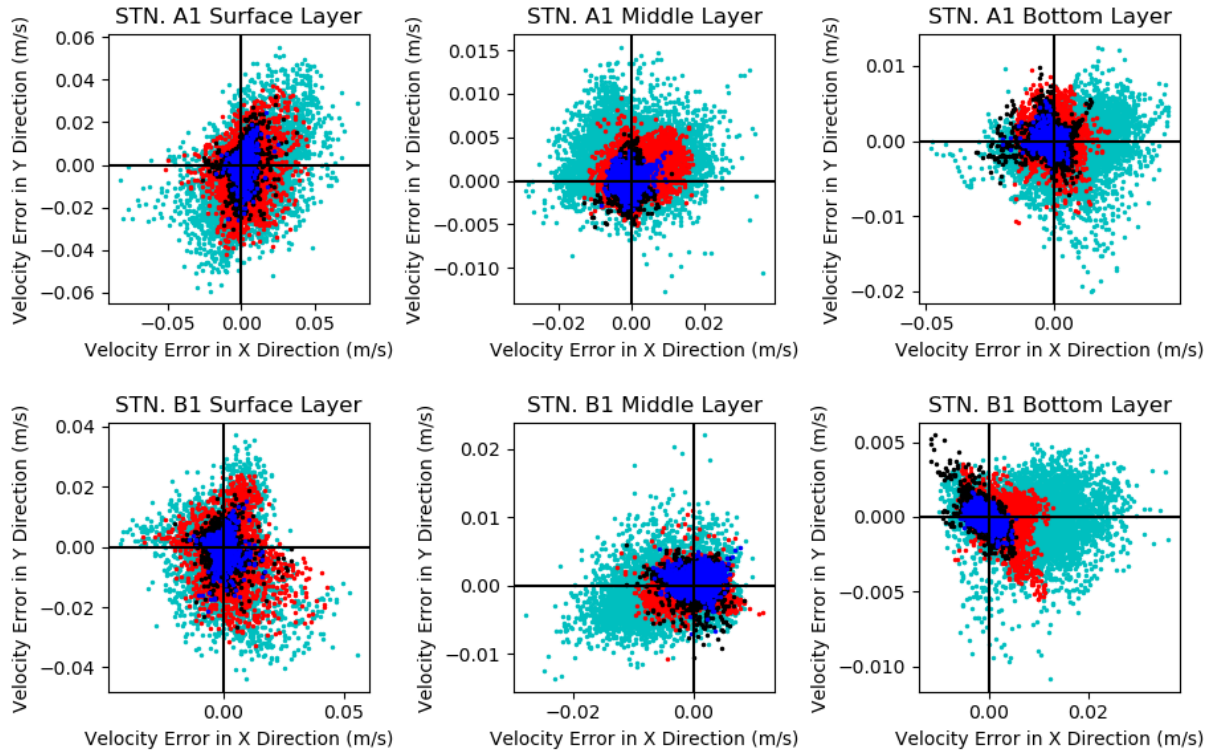
472
473

474 **Figure 3.** Scatter plot of velocity error $\Delta\overrightarrow{Vel}$ in horizontal (X and Y direction) between simulated velocity
475 $Sim_{t,j}^{\overrightarrow{Vel}}(\boldsymbol{X^*})$ and observed velocity $Obs_{t,j}^{\overrightarrow{Vel}}$ at location$j$.Each dot denotes the velocity error$\Delta\overrightarrow{Vel}$ of location j at
476 one time step. j = surface layer of STN. A1 for upper panel and j = STN. B1 for lower panel. $\boldsymbol{X^*}$is the optimal
477 solution found by PODS in each scenario: Cali-Tem (red dots); Cali-Vel (black dots) and Cali-Both (blue dots)
478 as listed in Table S1. The "True" solution is on or near the intersection of the two perpendicular black lines. An
479 initial uncalibrated solution (cyan dots) is plotted for reference.

480   Figure 4 shows the temperature error of solutions from three different calibration scenarios: Cali-Tem

481 (red time-series), Cali-Vel (black time-series) and Cali-Both scenarios (blue time-series). The errors between

482 simulated and observed water temperature at the surface, middle and bottom layers of two stations (STN. A1 and

483 STN B1) are plotted. In general, the temperature error of the solution in Cali-Both scenario is generally close to

484 zero °C for all the layers and stations shown. The solution in Cali-Tem scenario also got temperature error close

485 to zero °C at the middle and bottom layer at STN. A1, but it has larger temperature error than solution in the Cali-

486 Both at the surface layer of STN. A1 and all layers of STN. B1. The solution in the Cali-Vel scenario generally

487 overestimated the water temperature in all locations (i.e., all the surface, middle and bottom layers at both

488 stations). The temperature error of the solution in the Cali-Vel scenario is much larger than that of the solution in

489 Cali-Tem and Cali-Both scenarios in the middle and bottom layer of both stations. The temperature error at most

490 times, for the Cali-Vel scenario, is greater than 0.1 °C. This might be because both the Stanton and Dalton numbers

491 are underestimated in the Cali-Vel scenario when compared with the True solution ($\boldsymbol{X^R}$) (As shown in Fig. 5).

492 The Dalton number C_e affects the evaporative heat flux modeling and the Stanton number C_H influences the

493 convective heat flux modeling in the Delft3D-FLOW model (Hydraulics, 2006). For the solution in Cali-Vel, a

494 smaller Stanton number C_H(shown in Fig. 5) might lead to underestimated convective heat flux, which will lead

495 to the overestimation of the water temperature. In summary, calibrating to temperature and velocity (i.e., Cali-

496 Both) give the best solution in terms of temperature error compare with calibrating to temperature or velocity only

497 (i.e., Cali-Tem or Cali-Vel). Calibrating to velocity only (Cali-Vel) gives the worst result in terms of temperature

498   fit. Simulation of vertical temperature, vertical velocity, vertical eddy diffusivity, vertical eddy viscosity (Fig. S2-

499   S5) also shows that the solution in the Cali-Both scenario is much better than solutions in the Cali-Tem and Cali-

500   Vel scenario. For example, the solution in the Cali-Both scenario can almost capture the vertical time-varying

501   temperature profiles of the true solution. In contrast, calibrating to one variable did not fully capture the vertical

502   time-varying temperature profiles (e.g., April-May for Cali-Tem scenario; Mar-May and Aug-Sep for the Cali-

503   Both scenario in Fig. S2.) The solution in the Cali-Both scenario also give much smaller vertical velocity, eddy

504   diffusivity, and eddy viscosity error than solutions in other two scenarios (in Fig. S3-S5). The result indicates that

505   using both temperature and velocity data in model calibration also helps to improve the complex time-varying

506   vertical mixing behavior.

507
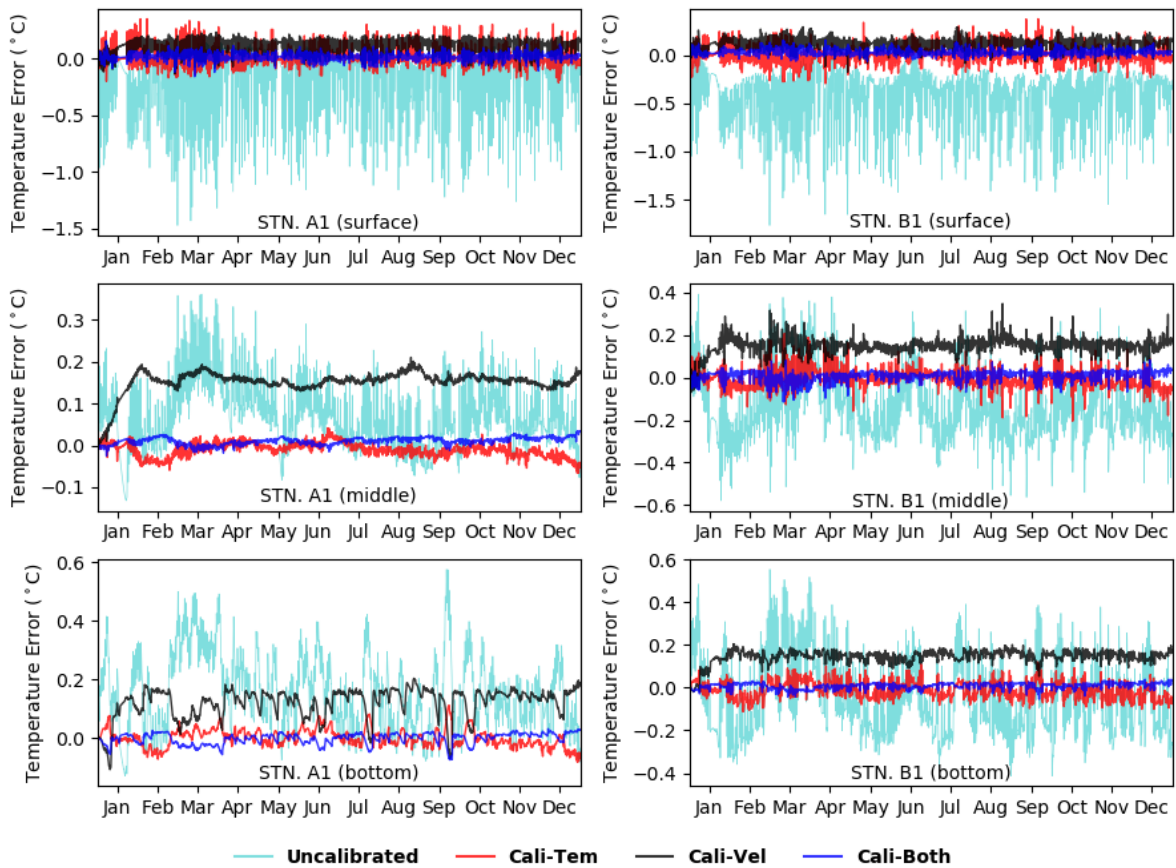
508
509   **Figure 4.** Time-series plots of temperature error ΔT between simulated water temperature and $Sim_{t,j}^{Tem}(X^*)$ and
510   observed water temperature ($Obs_{t,j}^{Tem}$) at location j where j = surface layer of STN4 for left panel and j = STN1
511   for the right panel. X^* is the optimal solution found by P-DYCORS in each scenario: Cali-Tem (Red lines); Cali-
512   Vel (Black lines) and Cali-Both (blue lines) as listed in Table S1. An initial uncalibrated solution (cyan lines) is
513   plotted for reference.

| v_H^{back} | D_H^{back} | v_V^{back} | D_V^{back} | L_{oz} | H_{Secchi} | c_e | c_H | n | $f_{Tem}(X)$ | $f_{\overline{Vel}}(X)$ |
| (m²/s) | (m²/s) | (m²/s) | (m²/s) | (m) | (m) | (-) | (-) | (m⁻¹/³/s) | | |
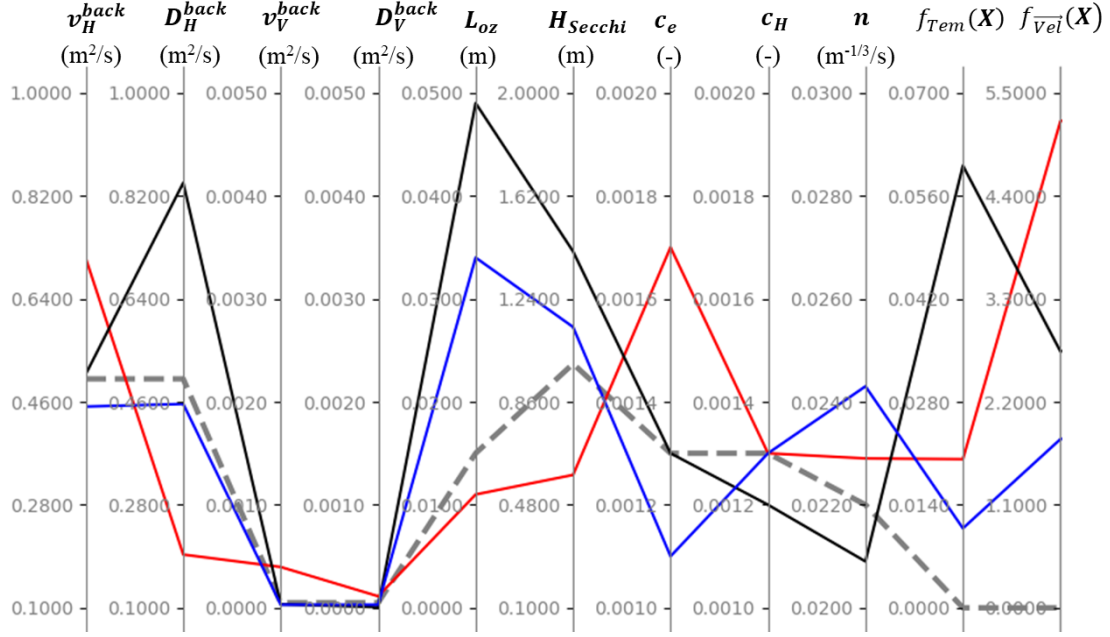
Figure 5. The parallel axis plot for the parameter value and the composite error of temperature and velocity of calibration solutions under different scenarios (Cali-Tem, Cali-Vel, and Cali-Both). True solution defined in Table 2 is given for reference. Smaller variable errors ($f_{Tem}(X)$ (see Eq. (7)) and $f_{\overline{Vel}}(X)$ (see Eq. (10))) are better, and the variable errors of the true solution (X^R) are zero (for both $f_{Tem}(X)$ and $f_{\overline{Vel}}(X)$). The parameter symbols are defined in Table2.

3.2 Optimization Search Dynamics under Different Calibration Scenarios

We further analyze calibration progress of PODS for Cali-Tem, Cali-Vel and Cali-Both, to understand the calibration convergence speeds of the three formulations. The purpose of the calibration progress analysis is to visualize the improvement in calibration quality of both temperature and velocity variables from the LHD, for all three formulations. As discussed in experiment setup section, we conducted 8 iterations of the optimization search. This is a reasonable number of iterations for our case given that 1) the problem is computationally expensive (one experiment takes about 64 hours to run and there are 9 experiments) and 2) the calibration progress plot in iterations (Figure S1) indicates that the optimization search almost converged in 8 iterations.

Figure 6 plots the calibration progress of the three formulations (i.e., Cali-Tem, Cali-Vel and Cali-Both) using PODS. Each subplot within Fig. 6, corresponds to the different concurrent optimization trials (i.e., trials of the stochastic optimization method using the same initial points from LHD) for each formulation. The best solutions are near the origin of each graph. Moreover, Fig. 6 plots the progress (quantified by visualizing both temperature and velocity errors) of the best solution found (measured in terms of the objective function value in each calibration scenario) during the search. Figure 6 indicates that when calibrating to temperature or velocity only, the optimization search cannot guarantee the improvement of the fit of another variable. For example, in Fig. 6 (a), when calibrating to velocity only, the temperature error of the best solution found at the end of the optimization search stage is worse than the temperature error of the best solution found after initial LHD, even though there is improvement in terms of velocity fit. Similarly, when calibrating to temperature only, the improvement on velocity fit is also not significant (for instance, in Fig. 6 (a)). When calibrating to the fit of both temperature and velocity using the DYNO formulation, the fit of both temperature and velocity improves in all trials, and the improvement remains balanced during the optimization search. Figure 6 also indicates that the final

solution found in Cali-Both scenarios dominates the best solution found by PODS in Cali-Tem and Cali-Vel in terms of both temperature and velocity fit.

Figure 6 also shows that when calibrating to one variable, the optimization search is easily convergent (i.e., the best solution does not continue improving after few iterations even in terms of the fit of the variable considered in calibration). For example, in Fig. 6(a), when calibrating to temperature only, the best solution in in terms of temperature error does not improve much (in the last few iterations). The reason might be that when the velocity error is large, it is less likely that the temperature fit would be improved further. In contrast, when calibrating to both temperature and velocity, the optimization search continues improving in both the temperature and velocity fit. Hence only considering one variable in the calibration, it is difficult to get a solution that have small (or close to zero) error of the variable considered. We should also highlight that even though the optimization get a solution that has zero error in one variable, it does not mean that the error of another variable would be zero. The reason is that only the observation in part of the simulation space is used for calibration (not the observation data at each grid and each time step of the simulation space are used to calculate the temperature error). So the temperature error may be 0 at these observation locations, while the temperature error is not 0 at other locations where observation is not used in calibration. In this case, getting a temperature error 0 at observation locations cannot guarantee the velocity error is 0.

(a) **(b)** **(c)**
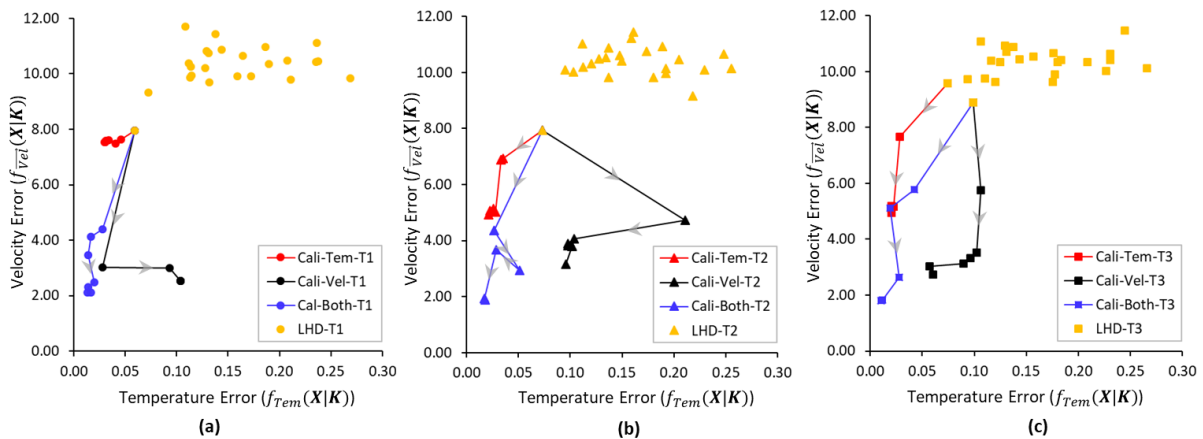
Figure 6. Calibration progress plot of the best solution found (in terms of objective function value) during optimization search by PODS when calibrating to temperature only (Cali-Tem), calibrating to velocity only (Cali-Vel), and calibrating to both temperature and velocity (Cali-Both). Three random trials (i.e., T1, T2, and T3) are plotted in (a), (b), and (c). Lower velocity and temperature error are better. The yellow makers are evaluation point in initial experiment design using LHD. Besides solutions in LHD, only the best solution in each of the optimization iterations is plotted (i.e., makers lined with lines). The line links the best previous solution in one iteration to the best solution in next iteration. The arrow indicates the direction from the previous solution to the next solution.

It is also important to understand the 'frequency' or likelihood with which PODS can find good temperature and velocity calibrations via the three different formulations proposed in this study. Hence, we also do a comparative frequency analysis of the errors (for velocity or temperature) of all evaluated points ($X_i, i = 1, ..., 3 \times N_{max}$) from all trials (3 trials) of PODS when using difference calibration formulations (see Table 3). The purpose of this frequency analysis is to understand the likelihood with which the three different formulations can obtain good velocity and temperature calibrations. The frequency analysis results are presented in Fig. 7 via visualizations of empirical histograms of both velocity error and temperature error (from all solutions of 3 trials of PODS) for each calibration scenario.
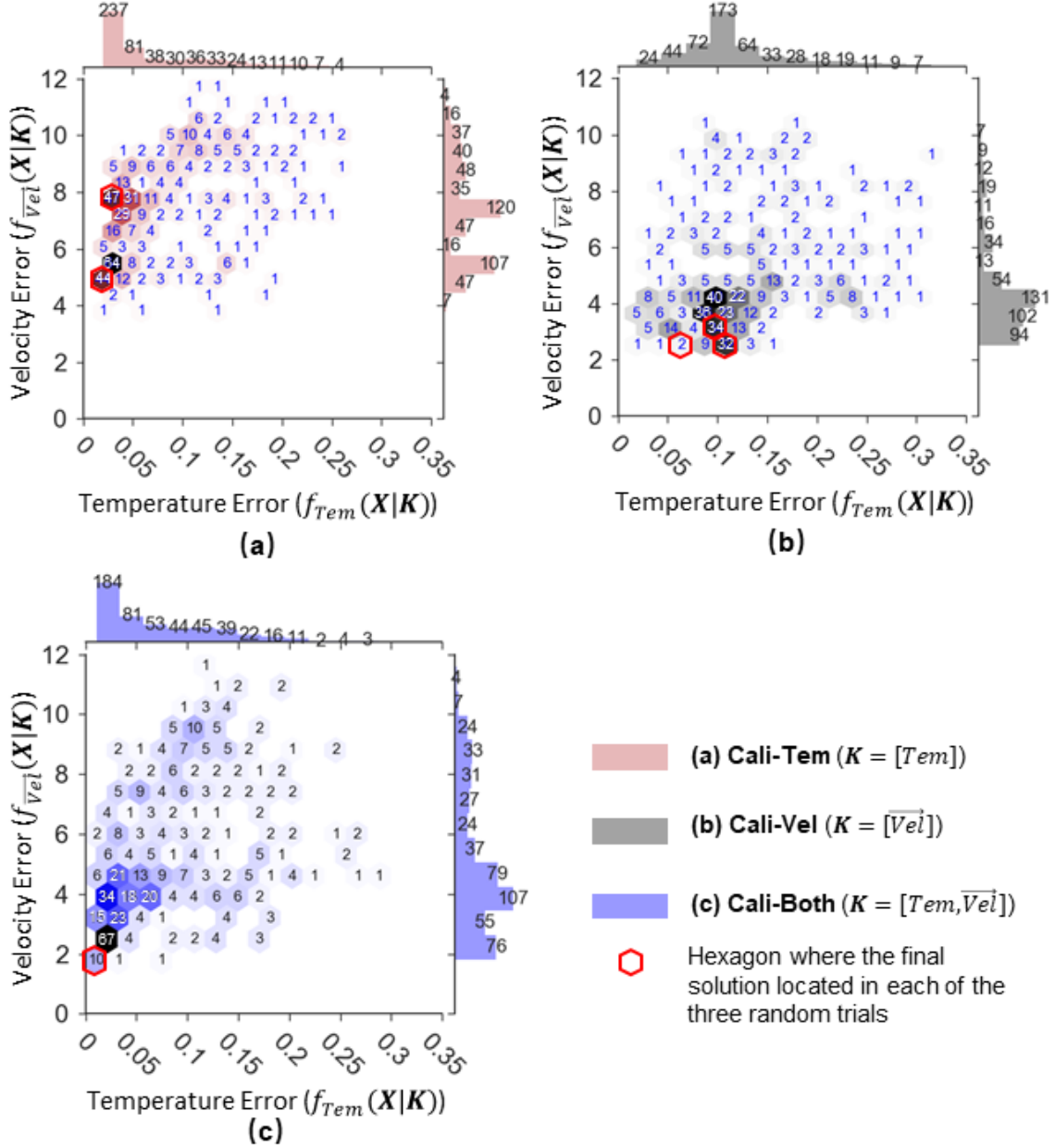
Figure 7. Distribution plot of all the evaluated points found by PODS (over 3 trials) in terms of temperature composite error $f_{Tem}(X|K)$ and velocity composite error $f_{\overrightarrow{Vel}}(X|K)$ in each scenario: Cali-Tem ($K = [Tem]$), Cali-Vel ($K = [\overrightarrow{Vel}]$), and Cali-Both ($K = [Tem, \overrightarrow{Vel}]$). The number inside each hexagon represent the number of evaluated points located in that hexagon (e.g. with the combination temperature and velocity error associated with the corresponding values on the axes.) Darker color in hexagon means larger number of evaluated points located in that hexagon. The bar plot along the upper x axis ($f_{Tem}(X|K)$) are the distribution of the evaluation points in terms of temperature error only. The bar plot along y axis ($f_{\overrightarrow{Vel}}(X|K)$) are the distribution of the evaluation points in terms of velocity error only. The number above the bar shows how many evaluated points located in that bin. Smaller error ($f_{Tem}(X|K)$ or $f_{\overrightarrow{Vel}}(X|K)$) is better. The true solution ($f_{Tem}(X^R|K), f_{\overrightarrow{Vel}}(X^R|K)$) is the origin of each subplot.

Figure 7 plots the error distribution of all the evaluated points over three trials (576 evaluations) for each

scenario: Cali-Tem ($K = [Tem]$), Cali-Vel ($K = [\overrightarrow{Vel}]$), and Cali-Both ($K = [Tem, \overrightarrow{Vel}]$). The different subplots

in Fig. 7 provide a visualization of the velocity (vertical axis) and temperature (horizontal axis) error distribution

via hexagonal bin (hexbin) plots (inside the square) and error histograms (outside the square) for each of the

calibration scenarios. The number inside each hexbin denotes the number of evaluated points (for that combination

590   of temperature error and velocity error) located in that hexbin. Furthermore, the hexbin with a larger number of

591   evaluated points is highlighted with a darker color shade. The temperature histogram columns (above the square)

592   represent the sum of all the hexbins inside the square directly beneath the number in the column. For velocity

593   histogram (on right side of square), the column height depends on the sum of all the hexbins in the row to the left

594   of the number.

595   The temperature and error velocity distribution visualizations of Fig. 7 clearly show that calibrating to

596   both temperature and velocity data (see Fig. 7 (c), i.e., error distribution for the Cali-Both scenario), provides good

597   temperature and velocity calibrations with a higher frequency. Figure 7 (c) shows that it is highly likely that both

598   temperature and velocity errors are lower (indicated by darker hexbins with temperature error $f_{Tem}(X|K)$ less

599   than 0.05 and velocity error $f_{\overline{Vel}}(X|K)$ less than 4). Consequently, Fig. 7(c) also illustrates that the newly

600   proposed DYNO (see Eq. (3)) works effectively, in this case, to calibrate multiple variables simultaneously.

601   Figure 7 also illustrates that it is better to calibrate the hypothetical hydrodynamic model to velocity data

602   rather than temperature data (see Fig. 7(a) and Fig. 7(b)) (if data for both variables is not available). Figure 7(a)

603   indicates that calibrating to temperature only (i.e., the Cali-Tem scenario) results in a high chance that velocity

604   error would be high (see the velocity error histogram in Fig. 7(a)). However, Fig. 7(b) illustrates that the errors in

605   temperature when calibrating to velocity only (Cali-Vel) are likely to be relatively small in magnitude (see the

606   temperature error histogram of Fig. 7(b)).

607   From the above discussion, we can conclude that calibrating to both temperature and velocity data with

608   the newly proposed DYNO (implemented within the efficient surrogate algorithm PODS) is effective in obtaining

609   a balanced calibration of both temperature and velocity variables. In real-world lake hydrodynamic applications,

610   if available, both temperature and velocity data should be used for lake hydrodynamic model calibration.

611   However, the very common practice of calibrating only to temperature data is shown to be unable to reproduce

612   the flow dynamics well. This supports extra effort and expense to collect velocity data is expected to give a

613   beneficial effect.

614   **3.3 Impact of Different Forms of Normalization on the Performance of DYNO**

615   This section investigates the impact of using different forms of normalization in the new objective function DYNO

616   on optimization search performance. In Eq. (3), the error of each variable is normalized by the maximum and

617   minimum values $f_k^{max}(X)$ and $f_k^{min}(X)$ of $f_k(X)$ among all the evaluations evaluated so far. One concern of

618   using the maximum value $f_k^{max}(X)$ is that the objective function can be affected by extremely bad evaluations

619   points. Another approach is to use the median value $f_k^{median}(X)$ of $f_k(X)$ among all the evaluations evaluated so

620   far as a replacement of $f_k^{max}(X)$ to normalize the error of each variable. We refer to DYNO using the median

621   value $f_k^{median}(X)$ as DYNO-N2 (as shown in Eq. (13)) to differentiate it from DYNO using the maximum value

622   $f_k^{max}(X)$ (as shown in Eq. (3)), which we refer to as DYNO-N1 in the following text.

623   $F(X|K) = \sum_{k \in K} \frac{f_k(X) - f_k^{min}(X)}{f_k^{median}(X) - f_k^{min}(X)}$ (13)

624   $f_k^{median}(X) = \text{med}\{f_k(X) \text{ for all } X \in \psi\}$ (14)

625

626   where $f_k^{median}(X)$ and $f_k^{min}(X)$ are the median and minimum values of $f_k(X)$ among all the evaluations

627   evaluated so far, and hence they are updated dynamically in each iteration during optimization.

628   The implementation of DYNO-N2 is similar to the implementation of DYNO-N1 (Eq. (3)). The only

629 change is replacing the calculation related to $f_k^{max}(X)$ with $f_k^{median}(X)$. We tested relative efficacies of DYNO-

630 N1 and DYNO-N2, by comparing three calibration trials, of each DYNO variant (using PODS), where each

631 concurrent calibration trial was initialized using the same LHD. Figure 8 shows the progress of PODS with the

632 two forms of DYNO as the objective functions. Figure 8 is similar in design to Fig. 6, and indicates that both

633 forms of DYNO are able to balance the calibration on temperature and velocity. There are two trials where PODS

634 with DYNO-N1 (using $f_k^{max}(X)$ for normalization) found a better solution than PODS with DYNO-N2 (using

635 $f_k^{median}(X)$ for normalization).

636   The results here indicate that DYNO-N1 seems not adversely affected by the bad solution. A reason for

637 this may be that PODS typically do not generate extremely bad solutions (i.e., outlier solutions with extremely

638 large errors), since algorithm search is concentrated around the best solution found so far. However, if other

639 optimization algorithms are used for calibration especially algorithms that explore the search space more, there

640 might be a higher likelihood of encountering outlier /extremely bad solutions during optimization search.

641 Consequently, the performance of such algorithm with DYNO-N2 might be better than with DYNO-N1, which

642 might need further investigation. The outlier solutions here mean solutions (obtained during the optimization

643 search phase) that have much larger errors than other solutions found so far. Outlier or extremely bad solutions

644 are also likely happen for calibration problems where the model output is very sensitive to the calibration

645 parameters (i.e., a small change in model parameters can cause huge changes in the model output that leads to

646 much worse solutions).
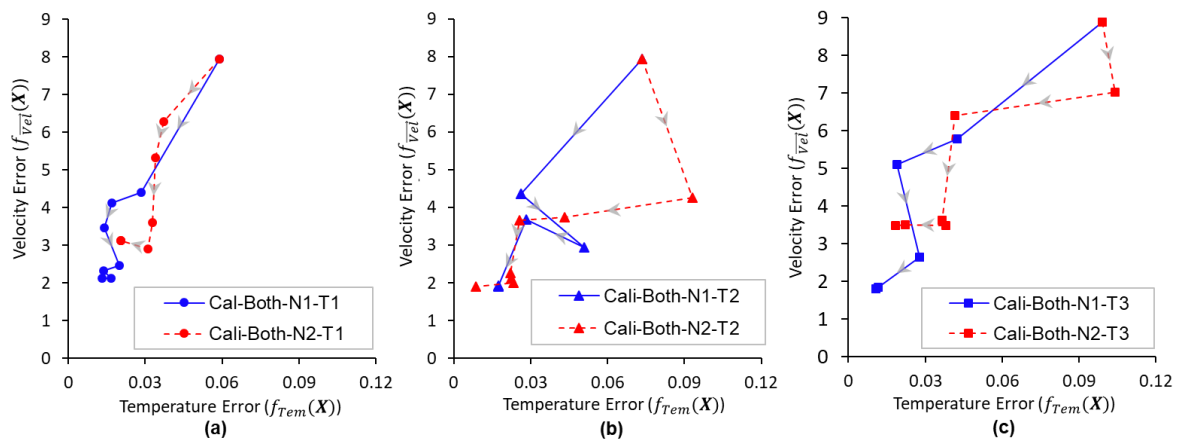
647

648 **Figure 8.** Calibration progress plot in terms of the best solution found during optimization search when using
649 DYNO-N1 and DYNO-N2 as the objective function. Three random trials (T1, T2, and T3) are plotted in (a), (b),
650 and (c). Lower velocity and temperature error are better. Figure 8 uses the same format as Figure 6.

651 **3.4 Value of Velocity Measures in 3D Lake Model Calibration**

652 High quality hydrodynamic simulations (e.g., thermal structure, current velocities, flow advection and vertical

653 mixing) are vital for accurate spatial modelling of water quality in lakes. The hydrodynamic process influences

654 the transport & production or transformation of biological and chemical components. Hence, if the simulation of

655 flow dynamics is not adequately accurate, there is no way to achieve accuracy in the simulation of water quality.

656 Previous studies use mostly temperature observations for the 3D lake hydrodynamic model calibration. Whereas,

657 velocity data is less commonly used compared with temperature data for model calibration.

658   Our results in section 3.1 indicate that calibrating to temperature data only cannot guarantee accuracy in
659 velocity simulation in our case. Not using velocity data in model calibration (i.e., using temperature data in model
660 calibration only) thus, may lead to large velocity errors (as indicated in the Fig. 3). The inclusion of velocity
661 measurements in calibration not only reduces velocity error but also helps improving the temperature fit. For
662 example, in Fig. 4, when calibrating to both temperature and velocity data, the temperature error is smaller than
663 the temperature error when calibrating to temperature data only. This is most obvious in the surface layers of both
664 STN. A1 and STN. B1, where the temperature error when calibrating to both temperature and velocity (i.e., Cali-
665 Both) is much smaller compared to calibrating to temperature only (i.e., Cali-Vel). The better result (better fit of
666 temperature as well as velocity) in Cali-Both demonstrates the effectiveness of using velocity measures in 3D
667 hydrodynamic lake model calibration. The comparison of calibrated parameter values in Cali-Both and Cali-Tem
668 scenarios (in Fig. 5) also demonstrates the value of using velocity data besides temperature data in model
669 calibration. In Fig. 5, we can see that the calibrated value of viscosity and diffusivity parameters in Cali-Both is
670 much closer to the true value than that in Cali-Tem. This shows that the use of velocity measures helps to improve
671 the calibration of these viscosity and diffusivity parameters. Our analysis is based on synthetic observation data
672 from the physical model since we don't have real velocity measurements. These physical models are based on
673 physics laws and knowledge from human's observation and understanding of environment. The analysis from
674 modelling can provide some implications for the real world situation. Hence, it is worthwhile to repeat the analysis
675 based on real data if there are real velocity measurements available in future.

676   The risk of using only temperature data without velocity data, even for accurately simulating water
677 temperature, is that temperature simulation is affected by both the flow dynamics and the heat transfer process.
678 The fit of temperature data is a result of the combination of these two processes. However, the fit of the
679 temperature data cannot guarantee accurate simulation of each of the processes, though accurate simulation of
680 each process does guarantee the fit of temperature data. The velocity observation hence is valuable to help improve
681 the flow dynamics simulation of the model, which is not only important for temperature simulation but also other
682 water quality substances simulation (e.g., biological and chemical components). Our research implication of the
683 use of velocity observations is also in line with the study of Baracchini et al. (2020), where they also suggest to
684 have both temperature and current velocity for a complete system calibration.

3.5 Possibilities for Other Applications

686 In this study, we only demonstrate how DYNO can be incorporated into PODS parallel surrogate global
687 optimization algorithm. (see section 2.6). However, the new objective function DYNO could also be easily
688 utilized with other heuristic optimization methods (e.g., serial or parallel versions of Genetic Algorithm (Davis,
689 1991) and Differential Evolution (Tasoulis et al., 2004)) for effectively calibrating other multi-variables
690 calibration problems. We have not provided a precise methodology for incorporating DYNO into other
691 optimization methods though, since incorporation of DYNO depends on the structure of an optimization method,
692 and structures of optimization methods vary a lot. We did illustrate in section 2.6 and Figure 3 on how components
693 of parallel PODS are modified in order to use DYNO. Other optimization methods could be modified in a similar
694 way to incorporate DYNO for use in multi-variable calibration.

695   Also, there are numerous other model calibration paradigms in general hydrology and water resources
696 (besides the hydrodynamic model calibration) where simultaneous multi-variable and multi-site calibrations are

required. Some examples of such multi-variable & multi-site calibration problems include watershed model calibration (Franco et al., 2020; Odusanya et al., 2019), seawater intrusion model calibration (Coulon et al., 2021), and water quality model calibration (Xia and Shoemaker, 2021) etc. In these problems, there are usually multiple constituents (e.g., substances) to be calibrated and the observations are usually available at multiple locations. Our new DYNO can potentially be used to calibrate them simultaneously. A popular calibration strategy for such problems in general hydrology is to use multi-objective calibration where it is assumed that a trade-off exists between multiple hydrologic responses (e.g., high flow, low flow, water balance, water quality etc.).

Using multi-objective algorithms, however, for calibrating hydrologic and watershed quality models may not be the most suited strategy for some case studies because i) multi-objective calibration can be computationally intensive if underlying simulations are computationally expensive and ii) meaningful trade-offs between different objectives may not exist. Kollat et al. (2012) demonstrate that prior multi-objective calibration exercises may have over-reported the number of meaningful trade-offs in hydrologic model calibration. DYNO is a reasonable alternative to classical multi-objective calibration in calibration problems where the trade-off between multiple component calibration objectives is not significant, because i) a balance between multiple constituent objectives is maintained with DYNO and ii) a single objective algorithm can be used with DYNO, which is computationally more efficient than a multi-objective algorithm. This is especially true for multi-constituent watershed model calibration problems where the achievable objective functions ranges for different constituents (e.g., flow, sediment, phosphorus etc.) are quite different. Multiple prior studies (Moriasi et al., 2012; Moriasi et al., 2015) highlight that achievable ranges of statistical calibration measures (e.g., Nash Sutcliffe Efficiency (NSE), bias etc.) are significantly different for different constituents (e.g., streamflow, sediment, total phosphorus etc.). Moriasi et al. (2015) note that in most watershed model case studies, the achievable range of NSE for streamflow is higher than the achievable range for total phosphorus. Hence, DYNO may be extremely effective in balancing simultaneous calibration of streamflow and phosphorus for such case studies. We believe that there is immense potential in the application of DYNO for multi-constituent watershed model calibration.

DYNO is also applicable to multi-constituent calibration problems where sampling locations and temporal frequencies for the different constituents are different. For instance, in real world hydrodynamic settings, it is very likely that sampling locations and frequencies of temperature and velocity observations are different. This is also true for watershed sampling settings, where sampling locations and frequencies for water quality (e.g. phosphorus) constituents are, typically, less than sampling distributions of streamflow. While the synthetic experiments of this study assume identical sampling locations & frequencies for temperature and velocity, DYNO requires the observations of multiple constituents (e.g., temperature and velocity in our case). It worth mentioning that DYNO does not require the same number of locations or same time frequency for different observation constituents. This is because DYNO first calculates the composite error of each constituents separately and then normalizes the composite error of each constituents dynamically, to balance the calibration of each constituent. This feature of DYNO allows it to be used in cases where different constituents are measured in different locations or time frequencies.

3.6 Future Work

Our analysis of the role of temperature and velocity measurements in 3D hydrodynamic model calibration is based on synthetic observation data generated from models. We do think it is worthwhile to further investigate the role

of temperature and velocity measurements in hydrodynamic model calibration if there are velocity measurements available in future.

Another possible future work is the consideration of the spatial-temporal variability of calibration parameters (such as Secchi depth, Ozmidov length scale, Dalton number, and Stanton number). We considered them as constant parameters in our study to simplify the problem. This is reasonable since our study area is relatively small and there is not much seasonal variation. In cases where the study areas are large and there is significant seasonal variation, there might be a need to consider these parameters as space and time-varying calibration parameters. The consideration of space and time variability will of course increase the number of decision variables for the optimization problems, which will bring more challenges. In that case, new methods on how to reduce the parameter dimensions might be needed (e.g., designing some low dimensional controlling parameters, like curve number in hydrology (Bartlett et al., 2016), to represent the high dimensional space-time variability of these parameters).

4 Conclusions

We conclude that the DYNO objective function that we propose is a new effective way to balance the calibration to different variables (i.e., temperature and velocity) in optimization-based -calibration. It is possible that the magnitudes of goodness-of-fit measures for different variables are very different (which may fluctuate during the optimization search), and thus the optimization search cannot maintain balance between different variables. Hence DYNO dynamically modifies the objective function, for multi-variable calibration, so that the error for each variable is being dynamically normalized in each iteration. This is to ensure that the search is giving approximately equal weight to each variable (e.g., velocity and temperature).

The proposed DYNO is tested in this study for simultaneous temperature and velocity calibration of a lake model. Moreover, DYNO is integrated with the PODS algorithm for testing on expensive lake hydrodynamic model calibration in parallel. Results indicate that using DYNO ensures a balanced calibration between temperature and velocity. We provide a detailed analysis to illustrate that DYNO balances the weight between different objectives dynamically, and thus allows for a balanced parameter search during optimization.

We conclude that calibrating to the error of one variable (either temperature or velocity) cannot guarantee the goodness-of-fit of another variable in our case. Of course, the most accurate predications can be obtained by having both temperature and velocity data. These comparisons are possible because we have, via synthetic simulation, the true solution for the lake model. Our analysis suggests that for practical applications, both temperature and velocity data might need to be considered for model calibration. The common practice of calibrating only to temperature data might not be sufficient to reproduce the flow dynamics accurately and extra effort and expense to collect velocity data is expected to give a beneficial effect. However, our analysis are based on synthetical data from models, hence it is worthwhile to further investigate the role of temperature and velocity in model calibration with real temperature and velocity measurements.

There are many possible future areas for application of this method. DYNO would be effective for other multi-variable and multi-site calibration problems (especially for problems with many variables). Future research could apply the DYNO methods on other problems and using other optimization algorithms.

Code and Data availability

The tropical reservoir hydrodynamic numerical model and data were provided by PUB, Singapore's National Water Agency (https://www.pub.gov.sg/). The Delft3D open source code could be downloaded from https://oss.deltares.nl/web/delft3d/source-code. The PODS open source code could be download from https://github.com/louisXW/PODS. The code for objective function can be download from https://github.com/louisXW/DYNO-pods.

Author contributions

WX took responsibility for the methodology, software, formal analysis, investigation, original draft preparation, and visualization. WX, TA, CAS discussed the design and results and edited the manuscript.

Competing interests

The authors declare that they have no conflict of interest.

Acknowledgments

This research was supported by the National Research Foundation, Prime Minister's Office, Singapore under its Campus for Research Excellence and Technological Enterprise (CREATE) programme and from Professor Shoemaker's start-up grant from the National University of Singapore (NUS). The authors acknowledge PUB, Singapore's National Water Agency for providing the tropical reservoir hydrodynamic numerical model and data. The computational work for this article was entirely performed on resources of the National Supercomputing Centre, Singapore (https://www.nscc.sg).

References

Afshar, A., Kazemi, H., and Saadatpour, M.: Particle swarm optimization for automatic calibration of large scale water quality model (CE-QUAL-W2): Application to Karkheh Reservoir, Iran, Water Resources Management, 25, 2613-2632, 2011.

Afshar, A., Shojaei, N., and Sagharjooghifarahani, M.: Multiobjective calibration of reservoir water quality modeling using multiobjective particle swarm optimization (MOPSO), Water resources management, 27, 1931-1947, 2013.

Akhtar, T. and Shoemaker, C. A.: Multi objective optimization of computationally expensive multi-modal functions with RBF surrogates and multi-rule selection, Journal of Global Optimization, 64, 17-32, 2016.

Alfonso, L., Jonoski, A., and Solomatine, D.: Multiobjective optimization of operational responses for contaminant flushing in water distribution networks, Journal of Water Resources Planning and Management, 136, 48-58, 2010.

Amadori, M., Giovannini, L., Toffolon, M., Piccolroaz, S., Zardi, D., Bresciani, M., Giardino, C., Luciani, G., Kliphuis, M., and van Haren, H.: Multi-scale evaluation of a 3D lake model forced by an atmospheric model against standard monitoring data, Environmental Modelling & Software, 139, 105017, 2021.

Ayala, A. I., Moras, S., and Pierson, D. C.: Simulations of future changes in thermal structure of Lake Erken: proof of concept for ISIMIP2b lake sector local simulation strategy, Hydrology and Earth System Sciences, 24, 3311-3330, 2020.

Baracchini, T., Hummel, S., Verlaan, M., Cimatoribus, A., Wüest, A., and Bouffard, D.: An automated calibration framework and open source tools for 3D lake hydrodynamic models, Environmental Modelling & Software, 134, 104787, 2020.

Bartlett, M., Parolari, A. J., McDonnell, J., and Porporato, A.: Beyond the SCS-CN method: A theoretical framework for spatially lumped rainfall-runoff response, Water Resources Research, 52, 4608-4627, 2016.

Bartz-Beielstein, T. and Zaefferer, M.: Model-based methods for continuous and discrete global optimization, Applied Soft Computing, 55, 154-167, 2017.

816 Beletsky, D., Schwab, D., and McCormick, M.: Modeling the 1998–2003 summer circulation and thermal
817   structure in Lake Michigan, Journal of Geophysical Research: Oceans, 111, 2006.
818 Chanudet, V., Fabre, V., and van der Kaaij, T.: Application of a three-dimensional hydrodynamic model to the
819   Nam Theun 2 Reservoir (Lao PDR), Journal of Great Lakes Research, 38, 260-269, 2012.
820 Coulon, C., Pryet, A., Lemieux, J.-M., Yrro, B. J. F., Bouchedda, A., Gloaguen, E., Comte, J.-C., Dupuis, J. C.,
821   and Banton, O.: A framework for parameter estimation using sharp-interface seawater intrusion models,
822   Journal of Hydrology, 600, 126509, 2021.
823 Davis, L.: Handbook of genetic algorithms, 1991.
824 Deltares: Delft3D-FLOW user manual, Deltares, Delft, the Netherlands2014.
825 Elhakeem, A., Elshorbagy, W., and Bleninger, T.: Long-term hydrodynamic modeling of the Arabian Gulf,
826   Marine Pollution Bulletin, 94, 19-36, 2015.
827 Fabio, P., Aronica, G. T., and Apel, H.: Towards automatic calibration of 2-D flood propagation models,
828   Hydrology and Earth System Sciences, 14, 911-924, 2010.
829 Franco, A. C. L., Oliveira, D. Y. d., and Bonumá, N. B.: Comparison of single-site, multi-site and multi-variable
830   SWAT calibration strategies, Hydrological Sciences Journal, 65, 2376-2389, 2020.
831 Galelli, S., Castelletti, A., and Goedbloed, A.: High-Performance Integrated Control of water quality and quantity
832   in urban water reservoirs, Water Resources Research, 51, 9053-9072, 2015.
833 Gaudard, A., Schwefel, R., Vinnå, L. R., Schmid, M., Wüest, A., and Bouffard, D.: Optimizing the
834   parameterization of deep mixing and internal seiches in one-dimensional hydrodynamic models: a case study
835   with Simstrat v1. 3, Geoscientific Model Development, 10, 3411-3423, 2017.
836 Giuliani, M., Castelletti, A., Pianosi, F., Mason, E., and Reed, P. M.: Curses, tradeoffs, and scalable management:
837   Advancing evolutionary multiobjective direct policy search to improve water reservoir operations, Journal of
838   Water Resources Planning and Management, 142, 04015050, 2016.
839 Gupta, H. V., Kling, H., Yilmaz, K. K., and Martinez, G. F.: Decomposition of the mean squared error and NSE
840   performance criteria: Implications for improving hydrological modelling, Journal of hydrology, 377, 80-91,
841   2009.
842 Haftka, R. T., Villanueva, D., and Chaudhuri, A.: Parallel surrogate-assisted global optimization with expensive
843   functions–a survey., Structural Multidisciplinary Optimization, 54, 3-13, 2016.
844 Herman, J. D., Zeff, H. B., Reed, P. M., and Characklis, G. W.: Beyond optimality: Multistakeholder robustness
845   tradeoffs for regional water portfolio planning under deep uncertainty, Water Resources Research, 50, 7692-
846   7713, 2014.
847 Huang, A., Rao, Y. R., Lu, Y., and Zhao, J.: Hydrodynamic modeling of Lake Ontario: An intercomparison of
848   three models, Journal of Geophysical Research: Oceans, 115, 2010.
849 Hui, Y., Zhu, Z., and Atkinson, J. F.: Mass balance analysis and calculation of wind effects on heat fluxes and
850   water temperature in a large lake, Journal of Great Lakes Research, 44, 1293-1305, 2018.
851 Hydraulics, D.: Delft3D-FLOW user manual, Delft, the Netherlands, 2006.
852 Jin, K.-R., Hamrick, J. H., and Tisdale, T.: Application of three-dimensional hydrodynamic model for Lake
853   Okeechobee, Journal of Hydraulic Engineering, 126, 758-771, 2000.
854 Kaçıkoç, M. and Beyhan, M.: Hydrodynamic and water quality modeling of Lake Eğirdir, Clean–Soil, Air, Water,
855   42, 1573-1582, 2014.
856 Lu, D., Ricciuto, D., Stoyanov, M., and Gu, L.: Calibration of the E3SM land model using surrogate-based global
857   optimization, Journal of Advances in Modeling Earth Systems, 10, 1337-1356, 2018.
858 Luo, L., Hamilton, D., Lan, J., McBride, C., and Trolle, D.: Autocalibration of a one-dimensional hydrodynamic-
859   ecological model (DYRESM 4.0-CAEDYM 3.1) using a Monte Carlo approach: simulations of hypoxic
860   events in a polymictic lake, Geoscientific Model Development, 11, 903-913, 2018.
861 Marti, C. L., Mills, R., and Imberger, J.: Pathways of multiple inflows into a stratified reservoir: Thomson
862   Reservoir, Australia, Advances in water resources, 34, 551-561, 2011.
863 Odusanya, A. E., Mehdi, B., Schürz, C., Oke, A. O., Awokola, O. S., Awomeso, J. A., Adejuwon, J. O., and
864   Schulz, K.: Multi-site calibration and validation of SWAT with satellite-based evapotranspiration in a data-
865   sparse catchment in southwestern Nigeria, Hydrology and Earth System Sciences, 23, 1113-1144, 2019.
866 Parsapour-Moghaddam, P. and Rennie, C. D.: Calibration of a 3D hydrodynamic meandering river model using
867   fully spatially distributed 3D ADCP velocity data, Journal of hydraulic engineering, 144, 04018010, 2018.
868 Paturi, S., Boegman, L., Bouffard, D., and Rao, Y. R.: Three-dimensional simulation of Lake Ontario North-Shore
869   hydrodynamics and contaminant transport, Journal of Hydraulic Engineering, 141, 04014082, 2014.
870 Pelletier, G. J., Chapra, S. C., and Tao, H.: QUAL2Kw–A framework for modeling water quality in streams and
871   rivers using a genetic algorithm for calibration, Environmental Modelling & Software, 21, 419-425, 2006.
872 Pijcke, G.: Water quality modelling for Gardens by the Bay, Singapore, National University of Singapore, 2014.
873 Råman Vinnå, L., Wüest, A., and Bouffard, D.: Physical effects of thermal pollution in lakes, Water Resources
874   Research, 53, 3968–3398, 2017.

875   Razavi, S., Tolson, B. A., and Burn, D. H.: Review of surrogate modeling in water resources, Water Resources
876   Research, 48, W07401, 2012.
877   Reed, P. M., Hadka, D., Herman, J. D., Kasprzyk, J. R., and Kollat, J. B.: Evolutionary multiobjective optimization
878   in water resources: The past, present, and future, Advances in water resources, 51, 438-456, 2013.
879   Regis, R. G. and Shoemaker, C. A.: A stochastic radial basis function method for the global optimization of
880   expensive functions, INFORMS Journal on Computing, 19, 497-509, 2007.
881   Regis, R. G. and Shoemaker, C. A.: Parallel stochastic global optimization using radial basis functions, INFORMS
882   Journal on Computing, 21, 411-426, 2009.
883   Regis, R. G. and Shoemaker, C. A.: Combining radial basis function surrogates and dynamic coordinate search in
884   high-dimensional expensive black-box optimization, Engineering Optimization, 45, 529-555, 2013.
885   Solomatine, D. P., Dibike, Y. B., and Kukuric, N.: Automatic calibration of groundwater models using global
886   optimization techniques, Hydrological Sciences Journal, 44, 879-894, 1999.
887   Soulignac, F., Vinçon-Leite, B., Lemaire, B. J., Martins, J. R. S., Bonhomme, C., Dubois, P., Mezemate, Y.,
888   Tchiguirinskaia, I., Schertzer, D., and Tassin, B.: Performance Assessment of a 3D Hydrodynamic Model
889   Using High Temporal Resolution Measurements in a Shallow Urban Lake, Environmental Modeling &
890   Assessment, 22, 309-322, 2017.
891   Tasoulis, D. K., Pavlidis, N. G., Plagianakos, V. P., and Vrahatis, M. N.: Parallel differential evolution,
892   Proceedings of the 2004 Congress on Evolutionary Computation (IEEE Cat. No. 04TH8753), 2023-2029,
893   Tolson, B. A. and Shoemaker, C. A.: Dynamically dimensioned search algorithm for computationally efficient
894   watershed model calibration, Water Resources Research, 43, 2007.
895   Uittenbogaard, R. E., Van Kester, J. T. M., and Stelling, G. S.: Implementation of Three Turbulence Models in
896   TRISULA for Rectangular Horizontal Grids: Including 2DV-testcases, Delft Hydraulics1992.
897   Wagner, C. R. and Mueller, D. S.: Use of velocity data to calibrate and validate two-dimensional hydrodynamic
898   models, Proceedings of the Second Federal Interagency Hydrologic Modeling Conference,
899   Wahl, B. and Peeters, F.: Effect of climatic changes on stratification and deep-water renewal in Lake Constance
900   assessed by sensitivity studies with a 3D hydrodynamic model, Limnology and Oceanography, 59, 1035-
901   1052, 2014.
902   Wilson, H. L., Ayala, A. I., Jones, I. D., Rolston, A., Pierson, D., de Eyto, E., Grossart, H.-P., Perga, M.-E.,
903   Woolway, R. I., and Jennings, E.: Variability in epilimnion depth estimations in lakes, Hydrology and Earth
904   System Sciences, 24, 5559-5577, 2020.
905   Xia, W. and Shoemaker, C.: GOPS: efficient RBF surrogate global optimization algorithm with high dimensions
906   and many parallel processors including application to multimodal water quality PDE model calibration,
907   Optimization and Engineering, 22, 2741-2777, 10.1007/s11081-020-09556-1, 2021.
908   Xia, W., Shoemaker, C., Akhtar, T., and Nguyen, M.-T.: Efficient Parallel Surrogate Optimization Algorithm and
909   Framework with Application to Parameter Calibration of Computationally Expensive Three-dimensional
910   Hydrodynamic   Lake   PDE   Models,   Environmental   Modelling   &   Software,   104910,
911   https://doi.org/10.1016/j.envsoft.2020.104910, 2021.
912   Xu, C., Zhang, J., Bi, X., Xu, Z., He, Y., and Gin, K. Y.-H.: Developing an integrated 3D-hydrodynamic and
913   emerging contaminant model for assessing water quality in a Yangtze Estuary Reservoir, Chemosphere, 188,
914   218-230, 2017.
915   Xue, P., Schwab, D. J., and Hu, S.: An investigation of the thermal response to meteorological forcing in a
916   hydrodynamic model of L ake S uperior, Journal of Geophysical Research: Oceans, 120, 5233-5253, 2015.
917